Chapter 1

Photo-nuclear interactions

In ultra-peripheral heavy-ion collision, the colliding nuclei interact only electromagnetically. In such events, no QGP state emerges, and the effects arising from the QGP no longer obscure the initial state effects. Other initial state probes such as peripheral nuclear collisions and proton-nucleus collisions have the potential to create the QGP obscuring which effects come from the initial state. In UPC events the nuclei do not collide, therefore final state effects coming from the QGP are not expected. Thus, UPC events provide clarity by enhancing physicists' understanding of the initial state.

In particular, these interactions between the field of photons surrounding the colliding nuclei and the gluons within the nuclei can produce a J/ψ, probing the gluon density. The J/ψ can be produced either coherently or incoherently. In the case of coherent interactions, the photon couples to the nucleus as a whole. In the incoherent case, the photon couples to the nucleons within the nucleus. The UPC J/ψ photoproduction cross section is therefore a probe of the initial state of the nucleus.

This cross section can be calculated using three steps. First, the Weizsäcker-Williams approximation provides a way to calculate the density of probing photons that surrounds the nucleus. Second, the electron-proton scattering data gives a value for the proton photoproduction cross section at lower energies [**?**]. Last, a specific model is used to combined the previous two steps in

order to calculate the nuclear photoproduction cross section. In this thesis the perterbutive Adeluyi and Bertulani (AB), STARlight, and the Leading Twist (LTA) models are discussed. Each of these methods handle the gluon density of the nucleus differently producing a measurable difference in the value of the J/ψ photoproduction cross section. Measurements at the LHC have provided important constrains to models of the nuclear gluon density. The analysis presented in Chapter 1 adds to the existing data in a new kinematic region. In this Chapter the theoretical framework for photon-nuclear interactions, together with an experimental review of recent results on ultra-peripheral heavy-ion collisions are described.

1.1 Weizsäcker-Williams approximation

The density of photons surrounding the colliding nuclei can be calculated using the Weizsäcker-Williams approximation. This approximation relates the electric field of a stationary point charge to the photon field that arises at ultra relativistic velocities. The approximation is semi-classical and combines both classical and quantum elements. In the Weizsäcker-Williams approximation, a Fourier transform of Maxwell's equations is combined with the quantum mechanical equation for the energy of the photon. The frequency modes of the electrostatic field are treated as photons. The

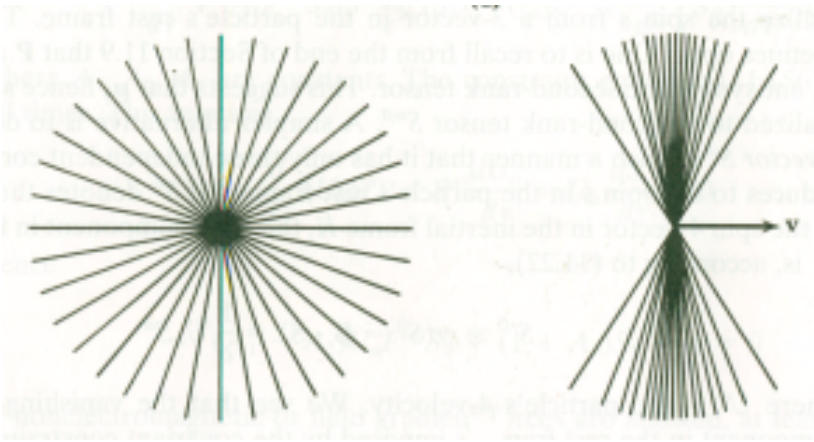

Figure 1.1: The electromagnetic field boosted and at rest.

Weizsäcker-Williams approximation makes the calculation of electromagnetic interactions with the

nucleus tractable.

The Weizsäcker-Williams approximation begins with the equation for the electric field of the projectile nucleus at rest. To calculate the photon flux on the target nucleus, the electromagnetic field only needs to be considered at the position of the target nucleus. From the projectile's point of view, the target is moving and contributes $-vt$ to Eq. **??**, the equation for the electric field of the projectile nucleus at rest.

$$x' = -vt', \qquad y' = b, \qquad z' = 0, \qquad \vec{\mathbf{E}}' = \left(\frac{eZ}{4\pi\varepsilon_0 \left((-vt')^2 + b^2 \right)^{3/2}} \right) \left(-vt'\hat{\mathbf{x}}' + b\hat{\mathbf{y}}' \right), \quad (1.1)$$

where b is the impact parameter defined as the distance of separation at closest approach, v is the velocity of the projectile nucleus, Z is the number of protons in the nucleus, and e is the charge of the electron. Two simplifications occur due to the choice of coordinates in Eq. **??**. The magnetic field is equal to zero, as the projectile is at rest, and the z coordinate can be ignored, reducing the equation to two dimensions.

The Lorentz transformation converts the field equations in the projectile's frame to equations in the target's frame. Eq. **??** gives the result of the transformation from the projectile's primed frame to the target's rest frame for the field components [**?**]:

$$\begin{aligned} E'_x = E_x, \qquad \gamma\left(E'_y/c + \beta B'_z\right) = E_y/c, \qquad \gamma\left(E'_z/c = \beta B'_y\right) = E_z/c, \\ B'_x = B_x, \qquad \gamma\left(B'_y - \beta E'_z/c\right) = B_y, \text{ and} \qquad \gamma\left(B'_z + \beta E'_y/c\right) = B_z. \end{aligned} \quad (1.2)$$

The transformation equations for the fields, Eq. **??**, and the transformation of the coordinates reduce to Eq. **??** [**?**]:

$$\begin{aligned} E'_x = E_x, \qquad \gamma E'_y = E_y, \qquad \gamma\beta E'_y/c = B_z, \\ ct' = \gamma ct, \text{ and} \qquad x' = -\gamma\beta ct. \end{aligned} \quad (1.3)$$

The Lorentz transformation reduces the six components of the electromagnetic field in the target's frame to the three equations in Eq. **??** by relating them to the fields in the projectile's frame.

By combining Eq. **??** and Eq. **??**, equations for the electric and magnetic fields in the target's rest frame are obtained

$$\vec{\mathbf{E}} = \left(\frac{\gamma e Z}{4\pi\varepsilon_0 \left((\gamma v t)^2 + b^2 \right)^{3/2}} \right) (vt\hat{\mathbf{x}} + b\hat{\mathbf{y}}), \text{ and}$$
$$\vec{\mathbf{B}} = \frac{\gamma\beta e Z b}{4\pi c\varepsilon_0 \left((\gamma v t)^2 + b^2 \right)^{3/2}} \hat{\mathbf{z}} = \frac{\gamma\mu_0 v e Z b}{4\pi \left((\gamma v t)^2 + b^2 \right)^{3/2}} \hat{\mathbf{z}}. \tag{1.4}$$

If the impact parameter b goes to zero, the target sits in the line of the projectile particle's motion, and the denominator carries a factor of γ squared. When vt goes to zero, the projectile particle position lays on the y-axis, and the numerator carries a factor of γ. This results in fields that are a factor of γ^3 higher in the y direction than in the x direction (see Fig. **??**). The boost compresses the electric field of the charge in the direction of the boost and produces a magnetic field resulting in a form similar to radiation. The point charge at ultra relativistic velocities produces a strong electric field in the plane transverse to its motion resembling a plane wave.

Separating the electromagnetic field into even and odd functions of time simplifies the decomposition of the field equations into Fourier frequency modes. The even functions decompose into cosine functions, odd functions into sine functions. The y-component of the electric field and the z-component of the magnetic field are even functions in time, and the x-component of the electric field is an odd function in time. Eq. **??** gives the Fourier transformation integrals.

$$E_x(\omega) = \sqrt{\frac{2}{\pi}} \frac{eZ}{4\pi\varepsilon_0 b^2} \int_0^\infty \frac{(\gamma v t/b)\sin(\omega t)}{\left((\gamma v t/b)^2 + 1 \right)^{3/2}} dt,$$
$$E_y(\omega) = \sqrt{\frac{2}{\pi}} \frac{\gamma e Z}{4\pi\varepsilon_0 b^2} \int_0^\infty \frac{\cos(\omega t)}{\left((\gamma v t/b)^2 + 1 \right)^{3/2}} dt, \text{ and} \tag{1.5}$$
$$B_z(\omega) = \frac{\beta E_y(\omega)}{c}.$$

The solutions to the integrals of Eq. **??** are the following [**?**]:

$$u = \frac{\gamma v t}{b}, \qquad du\left(\frac{b}{\gamma v}\right) = dt, \qquad \omega' = \frac{\omega b}{\gamma v},$$
$$\int_0^\infty \frac{u\sin(\omega' u)}{(u^2+1)^{3/2}} du = \omega' K_0(\omega'), \text{ and} \qquad \int_0^\infty \frac{\cos(\omega' u)}{(u^2+1)^{3/2}} = \omega' K_1(\omega'). \tag{1.6}$$

In Eq. **??**, ω can be related to the energy of a photon by $E = \hbar\omega$. The components of the electric field in terms of ω are:

$$E_x(\omega) = \sqrt{\frac{2}{\pi}} \frac{eZ}{4\pi\varepsilon_0 b^2} \frac{b}{\gamma v} \frac{\omega b}{\gamma v} K_0\left(\frac{\omega b}{\gamma v}\right), \text{ and} \qquad E_y(\omega) = \sqrt{\frac{2}{\pi}} \frac{\gamma eZ}{4\pi\varepsilon_0 b^2} \frac{b}{\gamma v} \frac{\omega b}{\gamma v} K_1\left(\frac{\omega b}{\gamma v}\right). \tag{1.7}$$

The y-component of the electric field does not have a factor of t in the numerator in Eq. **??**, therefore the factor of γ remains outside of the integral for the Bessel functions in Eq. **??**. In Eq. **??**, E_y carries an additional factor of γ in the numerator relative to the E_x, therefore in the case when $\gamma >> 1$, E_x can be neglected.

When v approaches c, $\beta \approx 1$, the y-component of the electric field and the z-component of the magnetic field are related by a factor of c, $E_y/c = B_z$. E_y is approximately equally to γE_x because $K_0(x)$ is smaller than $K_1(x)$ for all x. The conditions imposed by the ultra-relativistic limit result in the following relationship

$$\gamma \gg 1 \Rightarrow \gamma E_x \gg E_x \Rightarrow E_y \gg E_x. \tag{1.8}$$

The six field components are reduced to one electric component and one perpendicular magnetic field component, which have a configuration identical to a plane wave.

As with plane waves, the energy per area per time transferred by the electromagnetic field is given by the Poynting vector. The Poynting vector takes the simple form of a plane pulse propagating in the x direction as given by

$$\vec{\mathbf{S}} \equiv \vec{\mathbf{E}} \times \vec{\mathbf{B}}/\mu_0 = \left(E_y^2/c\mu_0\right)\hat{\mathbf{x}} = c\varepsilon_0 E_y^2 \hat{\mathbf{x}}. \tag{1.9}$$

The Poynting vector relates to the fluence (energy per unit area) by the expression [**?**]

$$I(b) = \hat{\mathbf{x}} \cdot \int_0^\infty \vec{\mathbf{S}} d\omega = \int_0^\infty \left(c\varepsilon_0 E_y^2\right) d\omega = \int_0^\infty \left(\frac{dI}{d\omega}\right) d\omega, \tag{1.10}$$

and the spectral fluence (energy per area per frequency) is given by

$$\frac{dI}{d\omega} = c\varepsilon_0 E_y^2 = \frac{e^2 Z^2 c}{4\pi^3 b^2 v^2 \varepsilon_0} \left(\frac{\omega b}{\gamma v}\right)^2 K_1^2\left(\frac{\omega b}{\gamma v}\right) = \alpha\hbar \left(\frac{Z}{b\beta\pi}\right)^2 \left(\frac{\omega b}{\gamma v}\right)^2 K_1^2\left(\frac{\omega b}{\gamma v}\right). \tag{1.11}$$

The spectral fluence given by Eq. **??** relates the frequency to energy. The quantum mechanical equation, $E = \hbar\omega$, gives the energy of a photon, which is related to the spectral fluence. The relationship between the photon number density and the spectral fluence is [**?**]

$$\frac{dI}{d\omega} d\omega = \hbar\omega N(\omega) d(\hbar\omega) \Rightarrow \frac{1}{\hbar^2\omega}\frac{dI}{d\omega} = N(\omega). \tag{1.12}$$

Substituting Eq. **??** into Eq. **??** yields the semiclassical photon flux:

$$N(\omega, b) = \frac{\alpha}{\hbar\omega}\left(\frac{Z}{b\beta\pi}\right)^2 \left(\frac{\omega b}{\gamma v}\right)^2 K_1^2\left(\frac{\omega b}{\gamma v}\right). \tag{1.13}$$

This replaces the classical electric field of a point charge with a semiclassical field of photons. The photon flux in Eq. **??** provides the electromagnetic input to the J/ψ photoproduction cross section calculation.

1.2 The STARlight model

The STARlight model for calculating the J/ψ photoproduction cross section has three main components. The STARlight approach is constructed from the Weizsäcker-Williams photon flux, uses the vector meson dominance fit to the proton-electron data, and uses the Glauber model for calculating the nuclear cross sections from the proton-electron cross sections. The Weizsäcker-Williams photon flux provides the probe. The proton-electron scattering data combine with the Glauber model

create a picture of the initial state of the nucleus. Each of the different approaches discussed in this thesis to calculating the UPC J/ψ photoproduction cross section use these same elements. However, the different models each use the last two elements differently to produce different pictures of the nucleus and different cross sections values.

The photon flux in the photoproduction cross section calculation must be finite in order for the cross section to be meaningful. The Weizsäcker-Williams approximation, Eq. **??**, diverges at $b = 0$. The probability of the nuclei interacting would exceed one if the photon flux were infinite. Special treatment of impact parameter, b, where the colliding nuclei overlap eliminates the divergency.

A convolution of the photon flux with the nucleon number density functions removes the divergency at $b = 0$. The nucleon density of a single nucleus is given by

$$\rho_A(s) = \frac{\rho_0}{1 + exp[(s - R_{WS})/d)]}, \tag{1.14}$$

where s is the distance from the center of the nucleus, R_{WS} is the radius of the nucleus, and d is the skin depth, which determines how quickly the nucleon density falls off beyond the nuclear radius. In Eq. **??** the depth of the nucleus is integrated out leaving just the transverse dimension in T_A. The average number of nucleons in the overlap region is given by a convolution of T_A from each of the two nuclei to produce The average number of nucleons in the overlap region is given by a convolution of T_A from each of the two nuclei to produce nuclear overlap integral, T_{AA},

$$\begin{aligned} T_A(\vec{r}) &= \int dz \rho_A(\sqrt{|\vec{r}|^2 + z^2}), \text{ and} \\ T_{AA}(|\vec{b}|) &= \int d^2\vec{r} T_A(\vec{r}) T_A(\vec{r} - \vec{b}). \end{aligned} \tag{1.15}$$

For a given impact parameter b, the product of $T_{AA}(|\vec{b}|)$ and σ_{NN} gives the average number of nucleon-nucleon collisions. It is T_{AA} that modulates the photon flux. As input to the Poisson distribution, T_{AA} reduces Eq. **??** at values of b where the nuclei overlap significantly and eliminates the divergency in the photon flux. The convolution of the photon flux with the b-dependent probability that no nucleon-nucleon collisions occur removes the divergency in Eq. **??**.

The Poisson distribution gives the probability that no collisions occur at a given b using the mean number of nucleons in the overlap region given by T_{AA}:

$$P_0(b) = exp[-T_{AA}(b)\sigma_{NN}], \tag{1.16}$$

where σ_{NN} is the cross section for a nucleon-nucleon interaction, which gives the probability that a collision will occur given the average number of nucleons in the overlap region. The photon flux is averaged over impact parameter by integration of the b-dependent photon flux multiplied by the b-dependent probability of having no nucleon-nucleon interactions:

$$\frac{dN_\gamma(k)}{dk} = \int_0^\infty 2\pi b db P_0(b) \int_0^R \frac{rdr}{\pi R_A^2} \int_0^{2\pi} d\phi \frac{d^3N_\gamma(k, b + r\cos(\phi))}{dkd^2r}. \tag{1.17}$$

Although Eq. **??** goes down to $b = 0$ where the photon flux is infinite, the fact that the probability of having a nucleon-nucleon collisions is high eliminates the divergency.

A power-law fit to the proton photoproduction data gives an analytic expression for the energy dependence of the proton photoproduction cross section. The fitting function depends on the photon-proton center of mass energy. The parameterization of the forward proton photoproduction cross section fit:

$$\frac{d\sigma(\gamma p \to Vp)}{dt}\Big|_{t=0} = b_v(XW^\varepsilon + YW^{-\eta}), \tag{1.18}$$

where W is the center of mass energy of the proton-photon system in Eq. **??**. The remaining variables in Eq. **??** are power-law fit parameters. The XW^ε term characterizes pomeron mediated interactions, and the YW^η term characterizes meson mediated interactions [**?**]. J/ψ's high mass relative to the π and ρ^0 renders the second term in Eq. **??** negligible as the term falls rapidly with increasing W. Eq. **??** allows for extrapolation and interpolation of the measured forward proton photoproduction cross section. The fit to the data provides estimates for energies that have not yet been probed experimentally. The proton photoproduction cross sections from the electron-proton scattering data is a direct input to the STARlight model. In this method, a power-law fit to the

proton photoproduction data is the input for the Glauber calculation.

Vector meson dominance and the optical theorem allow for the calculation of the total proton-meson scattering cross section from the fit given by Eq. **??**. The optical theorem relates the total cross section, σ, to the corresponding forward scattering cross section, $d\sigma/dt|_{t=0}$, where t is the momentum transfer squared. The most likely fluctuations of the photon are to vector mesons because of the quantum numbers of the photon. Due to this consideration, vector meson dominance asserts that only the vector meson fluctuations of the photon need to be considered. The forward scattering cross section is given by the following

$$\frac{d\sigma(\gamma p \to Vp)}{dt}\Big|_{t=0} = \frac{4\pi\alpha}{f_v^2(M_V, \Gamma_{l^+l^-})}\frac{d\sigma(Vp \to Vp)}{dt}\Big|_{t=0},$$
$$\sigma(Vp)^2_{tot} = 16\pi\frac{d\sigma(Vp \to Vp)}{dt}\Big|_{t=0}, \tag{1.19}$$

where M_V, is the mass of the vector meson, and $\Gamma_{l^+l^-}$, is leptonic decay width. The result of combining vector meson dominance and the optical theorem in Eq.**??** provides the cross section for a meson to scatter off a proton.

The Glauber model allows for Eq. **??**, the proton-meson scattering cross section, to be used to calculate a nucleus-meson scattering cross section. The Glauber model is used to calculate nuclear cross sections from nucleon interaction cross sections by use of T_{AA}. The combination of the mean number of nucleons in the overlapping region of a nucleus-nucleus collision, T_{AA}, the nucleon cross section, σ, and the Poisson distribution make-up the core of the Glauber model. For the total nucleus-meson scattering cross section, the equation has the following form:

$$\sigma_{tot}(VA) = \int d^2\vec{r}(1 - e^{-\sigma_{tot}(Vp)T_{AA}(\vec{r})}). \tag{1.20}$$

In Eq. **??**, the term $e^{\sigma_{tot}(Vp)T_{AA}}$ gives the probability of having no meson-nucleon scatterings from the Poisson distribution. The probability of having at least one scattering is given by subtracting one from the term $e^{\sigma_{tot}(Vp)T_{AA}}$ in Eq. **??**.

Reversing the process used for the proton, Eq. **??**, the meson nucleus scattering cross section, relates to forward nuclear photoproduction cross section through the optical theorem. Using the optical theorem, the nuclear photoproduction cross section is given by

$$\frac{d\sigma(\gamma A \to VA)}{dt}\Big|_{t=0} = \frac{\alpha\sigma_{tot}^2(VA)}{4\pi f_v^2},$$
$$\sigma(\gamma A \to VA) = \frac{d\sigma(\gamma A \to VA)}{dt}\Big|_{t=0}\int_{t_{min}}^{\infty} dt|F(t)|^2, \tag{1.21}$$

where F is the Fourier transform of the nuclear density function, ρ_A. Eq. **??** is joined with the photon flux incident on the nucleus resulting in the following

$$\sigma(AA \to AAV) = 2\int dk\frac{dN_\gamma}{dk}\sigma(\gamma A \to VA). \tag{1.22}$$

The factor of 2 in Eq. **??** comes from the fact that both of the two colliding nuclei contribute. Vector meson production rates in UPC collisions can be calculated by Eq. **??**. In this thesis the measured UPC J/ψ cross section is compared to the STARlight predictions.

1.3 The Adeluyi and Bertulani model

To calculate the UPC J/ψ photoproduction cross section, the Adeluyi and Bertulani model uses the nuclear gluon density to characterize the nucleus and the Weizsäcker-Williams approximation for the probing photon flux. The AB method combines these components such that the nuclear gluon density is a direct variable. The nuclear gluon density term in the AB formulation allows for the use of a variety of nuclear gluon density models. A range of nuclear gluon densities are present in the available models resulting in a wide range of possible cross section values. The UPC J/ψ photoproduction cross section is correlated with the gluon density of the nucleus, increasing with higher densities and decreasing with lower densities. In the AB approach, the calculation of the UPC J/ψ photoproduction cross section allows experiments to constrain many different nuclear gluon density models.

In the AB method, the photon interacts with the nucleus by fluctuating to a quark-anitquark pair. For J/ψ, the photon fluctuates to a $c\bar{c}$ pair. The probability for the photon to fluctuate to a $c\bar{c}$ pair depends on the $M_{J/\psi}$, the mass of J/ψ, $\Gamma_{l^+l^-}$, the J/ψ leptonic decay width, and α, the electromagnetic coupling constant. These three variables connect the c quark to the electromagnetic force mediator, the photon. Recast as a $c\bar{c}$ pair, the photon couples to the nuclear gluon density. The AB method uses the fluctuation of the photon to a $c\bar{c}$ pair as the foundation for calculating the forward J/ψ photoproduction cross section.

The $c\bar{c}$ pair arising from the photon fluctuation scatters off the gluons of the nucleus. The density of gluons in the nucleus determines how likely and therefore how large the cross section is for the quarks to scatter and form a J/ψ. The forward scattering cross section is the portion of those scattering events which transfer the minimum amount of momentum between the photon and the nucleus. The forward cross section for J/ψ photoproduction in the nucleus has the following form [**?**]:

$$\frac{d\sigma_{\gamma A\to J/\psi A}}{dt}\bigg|_{t=0} = \xi_{J/\psi}\Big(\frac{16\pi^3\alpha_s^2\Gamma_{l^+l^-}}{3\alpha M_{J/\psi}^5}\Big)[xG_A(x,\mu^2)]^2, \tag{1.23}$$

where $\xi_{J/\psi}$ is an experimentally derived correction factor, α_s is the strong coupling constant, x is the momentum faction of the nucleus the scattering gluons carry, and G_A is the gluon density of the nucleus. Both the c and $\bar{c}$ couple to the gluon density, and the double coupling results in the squared dependence of the cross section on the gluon density in Eq. **??**. Fitting Eq. **??** to proton-electron scattering data sets $\xi_{J/\psi}$ [**?**]. The forward scattering cross section given by Eq. **??** connects the photon flux to the gluon density and provides the input to calculate the total cross section by the optical theorem.

The optical theorem relates the forward cross section in Eq. **??** to the total photoproduction cross section. The total cross section gives the probability that a photon incident on the nucleus will produce a J/ψ regardless of the momentum transfered in the interaction. The total cross section

equation is given by

$$\sigma_{\gamma A\to J/\psi A}(k) = \frac{d\sigma_{\gamma A\to J/\psi A}}{dt}\Big|_{t=0}\int_{t_{min}(k)}^{\infty} dt|F(t)|^2, \tag{1.24}$$

where $t_{min} = (M_{J/\psi}^2/4k\gamma_L)^2$, which is the minimum amount of momentum transfer required to produce a J/ψ given the photon wave number k. The k dependence of t_{min} translates to the rapidity dependence of the total cross section. The total cross section for photoproduction, Eq. **??**, provides the input to Eq. **??**, which gives the rapidity dependence of the UPC photoproduction cross section. Eq. **??** as input to Eq. **??** allows for experimental comparison of the AB method to measurements of UPC photoproduction cross sections. With the AB method's direct use of the nuclear gluon density in Eq. **??**, the AB method allows for experimental exploration of any gluon density model.

1.4 Leading Twist Approach Derivation

The Leading Twist Approach is another method for calculating UPC photoproduction cross sections. Contrary to the STARlight model, the LTA model introduces additional nuclear effects originating from modification of the nuclear gluon density. The LTA method uses the Weizsäcker-Williams approximation to calculate the photon flux created by the colliding nuclei. As in the STARlight method, the probability of having no hadronic collisions modulates the flux. The photon flux for the LTA method has the following form [**?**]:

$$n_{\gamma/A}^i(\omega_\gamma) = \frac{2\alpha Z^2}{\pi}\int_{b_{min}}^{\infty} db\frac{x^2}{b}\Big[K_1^2(x) + \frac{K_0^2(x)}{\gamma_L^2}\Big]P_0(b)P_C^i(b), \tag{1.25}$$

where $x = \frac{\omega b}{\gamma_L}$, and $K_0^2(x)$ term contributes a photon flux in the transverse direction, and $P_C^i(b)$ is an modulation factor that requires various additional interactions. These interactions result in emission of neutrons from the receding nuclei as the nuclei relax from excited states. The terms P_C^i and K_0 provide additional ways to distinguish UPC events from nuclear collisions experimentally but leave the underlying interaction mechanism the same. For example, the additional terms in the

LTA formulation of the photon flux produce calculations of asymmetric neutron emission, which separate UPC events from nuclear collisions.

The LTA model derives the nucleon cross section from derivations of the nucleon gluon densities from electron-proton scattering data and leading order perturbative quantum field theory calculations. The forward photoproduction cross section of the nucleon has the following form [**?**]:

$$\frac{d\sigma_{\gamma N\to J/\psi N}(t=0)}{dt} = \frac{16\Gamma_{l^+l^-}\pi^3}{3\alpha M_{J/\psi}^5}[\alpha_s\mu^2 x G_N(x,\mu^2)]^2, \tag{1.26}$$

where G_N is the gluon density of the nucleon, x is the fraction of the nucleon's momentum the gluon carries, and μ is related to momentum at which the nucleon is being probed, which is equal to $M_{J/\psi}/2$ for J/ψ photoproduction. By connecting the gluon density to the cross section, Eq. **??** allows for the gluon density to be experimentally probed.

The LTA model exploits the optical theorem to relate the forward photoproduction cross section of the nucleon to the nuclear cross section. The relation is

$$\sigma_{\gamma A\to J/\psi A}(\omega) = \frac{d\sigma_{\gamma N\to J/\psi N}}{dt}(\omega,t_{min})R_g^2\int_{t_{min}}^{\infty} dt|F(t)|^2, \tag{1.27}$$

where R_g is the nuclear modification function, the ratio between the gluon density of the nucleon, G_N, to the gluon density of the nucleus, G_A. As with the STARlight method, the optical theorem relates the forward cross section, $\frac{d\sigma_{\gamma N\to J/\psi N}}{dt}(\omega,t_{min})$, to the total cross section, $\sigma_{\gamma A\to J/\psi A}$.

From Eq. **??**, the LTA method can predict the angular distribution of photoproduced J/ψ with respect to the beam axis. The angular distribution is expressed in the form of the rapidity dependency of the UPC photoproduction cross section given by

$$\frac{d\sigma_{A_1A_2\to A_1A_2J/\psi}}{dy} = n_{\gamma/A_1}(y)\sigma_{\gamma A_2\to J/\psi A_2}(y) + n_{\gamma/A_2}(-y)\sigma_{\gamma A_1\to J/\psi A_1}(-y), \tag{1.28}$$

where $y = ln\left(\frac{2\omega}{M_{J/\psi}}\right)$. Eq. **??** is comprised of two terms, one for photons from the forward going nucleus interacting with the backward going nucleus, and a second for the reverse situation. The

integration of Eq. **??** over y produces the factor of 2 that is present in Eq. **??**. The rapidity distribution of the photoproduction cross section given in Eq. **??** provides a more detailed prediction and allows for more direct experimental comparisons.

1.5 Photon-induced nuclear break-up

In addition to the photoproduction of quark anti-quark resonances such as the J/ψ, photo-nuclear interactions can also result in emission of a neutron from the struck target nucleus. To calculate the cross section for neutron emission in UPC events, the photon flux calculated from the Weizsäcker-Williams approximation is combined with the nuclear photon absorption cross section. The absorption of photons can be described by two processes, namely the Giant Dipole Resonance (GDR), and the dissociation of deuterium. In this section, the theoretical description of photon-induced nuclear break-up is discussed.

Following the formulation in [**?**], the cross section for a nucleus to absorb a photon, σ_{PN}, is given by

$$\sigma_{PN} = \sigma_{GDR} + \sigma_{QD}. \tag{1.29}$$

The Giant Dipole Resonance (GDR) cross section, σ_{GDR} is the result of the collective motion of the protons relative to the neutrons and dominates at lower photon frequencies. The Quasi-Deuterium (QD) cross section, σ_{QD}, represents the nucleus as a collection of proton-neutron pairs (deuterium) and dominates at higher photon energies.

There are two models for the GDR: the Goldhaber and Teller model, and the Steinwedel and Jensen model. Goldhaber and Teller treats the protons and neutrons as two separate and ridged density profiles that, when excited, oscillate with respect to each other [**?**]. Steinwedel and Jensen modeled the protons and neutrons as fluids contained in a single sphere that have shifting density profiles [**?**].

In the Goldhaber and Teller model, the potential that holds protons and neutrons together depends on the difference of the neutron and proton densities squared. Assuming the neutron and

proton densities have the same shape, if the two fully overlap, there is no difference in the densities and the potential energy is zero. If the two density distributions are separated, the overlap in the shape will not cancel. In the separated configuration, there will be a non-zero potential energy. The potential energy has the form of a harmonic oscillator with a spring constant that depends on the initial density distribution [**?**] given by

$$U = \frac{1}{2}Kz^2, \qquad K = k\int d^3r\,(\nabla\rho_0)^2\,. \tag{1.30}$$

If the nucleus has a shape cut off in density at its edge, then the integral is dominated by the region at the surface, and the spring constant, K, becomes proportional to $A^{2/3}$, where A is the mass number of the nucleus. The surface area of a sphere is proportional to its volume to the 2/3 power explaining the mass dependence. Due to this dependence, the frequency of the giant dipole resonance in the Goldhaber and Teller model is given by

$$\omega = \sqrt{\frac{K}{M}} \propto \sqrt{\frac{A^{2/3}}{A}} = A^{-1/6}. \tag{1.31}$$

This dependence describes light nuclei well, but it does not describe heavier nuclei [**?**]. The Steinwedel and Jensen model can be used to describe heavier nuclei. In this model, the proton and neutron fluids are confined to a single sphere where they are allowed to slosh back and forth creating the same effect as the Goldhaber and Teller model. Here there is no global separation of the proton and neutron fluids. The dipole is created by under-densities and over-densities of the proton and neutron fluids. It can be shown that this results in a frequency of oscillation which depends on one over the radius of the nucleus [**?**]:

$$\omega \propto \frac{1}{R} \propto A^{-1/3}. \tag{1.32}$$

As before, the relationship in Eq. **??** arises from the geometry of a sphere. The dependence of the giant dipole resonance that is seen in the Steinwedel and Jensen model describes medium and

heavier mass nuclei well. Empirically, both models are put together to give the following mass number dependence of the dipole resonance [**?**]

$$E_{GDR} = 32.2A^{-1/3} + 20.6A^{1/6}. \tag{1.33}$$

In order to compute the effect of an excitation in either model, the harmonic oscillator solutions found earlier can be driven by an interacting force. The resulting differential equation can then be solved using a Fourier transform to eliminate the time derivatives. In this model the driven harmonic has the following Lorentzian form:

$$\sigma_{GDR}(E_\gamma) = \frac{\sigma_{max} E_\gamma \Gamma_{GDR}^2}{\left(E_\gamma^2 - E_{GDR}^2\right)^2 + E_\gamma^2 \Gamma^2}, \tag{1.34}$$

where σ_{max} is the maximum cross section reached when $E_\gamma = E_{GDR}$; E_{GDR} is the peak resonance energy, and Γ_{GDR} is the width of the resonance. The width of this distribution lies in a range from 4-8 MeV and depends on the orbital arrangement to the neutrons and protons in the given nucleus [**?**].

For higher energy photons, the quasi-deuterium cross section is needed. The nucleus is treated as a collection of proton-neutron pairs, which are screened by the rest of the nucleus, in the quasi-deuterium approach. This behavior is modeled by [**?**]

$$\sigma_{QD}(E_\gamma) = L\frac{(L-A)Z}{A}\sigma_d(E_\gamma)F(E_\gamma), \tag{1.35}$$

where σ_d is the deuterium disintegration cross section for $\gamma + d \rightarrow p + n$; F is a function from Pauli blocking of fermions, and L is an empirical parameter set by data to 6.5 [**?**]. Certain energy levels are not available to the products of the deuterium disintegration process because of the presence of the rest of the nucleus. The result is a reduction of the cross section relative to free deuterium.

F can be modeled with an exponential cutoff below 20 MeV, a polynomial in the intermediate range with nearly linear dependence on E_γ, and an inverted exponential above 140 MeV, pushing F

to one at higher values of E_γ [**?**]. Essentially, the model at low photon energies disallows deuterium disintegration because the products have no available state to occupy, and at high energies the rest of the nucleus becomes transparent and looks more and more like a collection of deuterium. The deuterium disintegration cross section is found empirically and is fit to the following function [**?**]:

$$\sigma_d(E_\gamma) = 61.2\left(E_\gamma - 2.224\right)^{3/2}/E_\gamma. \tag{1.36}$$

In order to produce a final state for the target nucleus, a branching ratio is needed. The branching ratio gives the probability that the photo-excited nucleus will end up in a particular state. This determines the sort of emission that will result from the de-excitation process [**?**].

All the tools are now assembled to calculate the cross section for neutron emission. The first step in the calculation is to assume that the number of photons absorbed by either nucleus in the collision obeys the Poisson distribution [**?**, **?**]. The average number of absorptions as a function of impact parameter, $m(b)$,

$$m(b) = \int_{\omega_{min}}^{\omega_{max}} N(\omega, b)\sigma_{PN}(\omega)d\omega. \tag{1.37}$$

where σ_{PN} is the photo-nuclear cross section, and N is the photon flux (see Eq. **??**).

In [**?**], the probability of any final state i due to the absorption of a single photon is given by

$$P_i(b) = \int_{\omega_{min}}^{\omega_{max}} P_a(b,1)q(b,\omega)f_i(\omega)d\omega = e^{-m(b)}\int_{\omega_{min}}^{\omega_{max}} N(b,\omega)\sigma_{PN}(\omega)f_i(\omega)d\omega, \tag{1.38}$$

where P_a is the probability that the target absorbs a single photon as calculated by following the Poisson distribution; q is the probability that the photon will have the frequency ω, and f_i is the branching ratio to a given final state. The following equation describes q [**?**]

$$q(b,\omega) = \frac{N(b,\omega)\sigma_{PN}(\omega)}{m(b)} \tag{1.39}$$

Integrating over the impact parameter to get an area that is weighted by the probability func-

tions gives [**?**, **?**]

$$\sigma_i = 2\pi \int_{b_0}^{\infty} bP_i(b)db. \tag{1.40}$$

Three parameters arise when calculating the cross section in Eq. **??**, the minimum impact parameter b_0, the minimum emitted photon frequency ω_{min}, and the maximum emitted photon frequency ω_{max}. A minimum impact parameter ensures that the Bessel function in the photon flux in Eq. **??** is not evaluated at zero. At zero, the modified Bessel function does not converge. Physically, a minimum impact parameter is selected in order to separate the domains between electromagnetic interactions and the strong interactions that happen inside the nucleus. To serve this end, the minimum impact parameter is set to the radius of the nuclei [**?**, **?**]. This excludes collisions where the nuclei overlap in the calculation, and ensures that only electromagnetic interactions are involved.

1.6 Experimental Results

1.6.1 UPC measurements at RHIC

One of the first results from RHIC was a UPC measurement, the measurement of the neutron spectrum from photon-induced nuclear break-up [**?**]. Neutrons due to the nuclear photon absorption are emitted with momenta on the order of the giant dipole resonance, about 60 MeV. Momenta of 60 MeV compared to the 100 GeV beam energy at RHIC result in neutron emission at very small angles, $\sim$ 2mrad, relative to the beam. These neutrons are captured by calorimeters, which are set in line with the beam called Zero Degree Calorimeters (ZDCs). These detectors are described in Section **??**. Figure **??** shows the charge recorded by the ZDCs. The peak at $\sim$ 30 in Fig. **??** is due to emission of a single neutron. Each successive peak is due to emission of an additional neutron. From these peaks, the cross section for nuclear break-up by neutron emission by both nuclei was measured. The fraction of nuclear interaction in all events with neutrons on both sides of the interaction point was found to be 0.661 ± 0.014 [**?**], which is in agreement the value 0.659 predicted by the model described in [**?**].

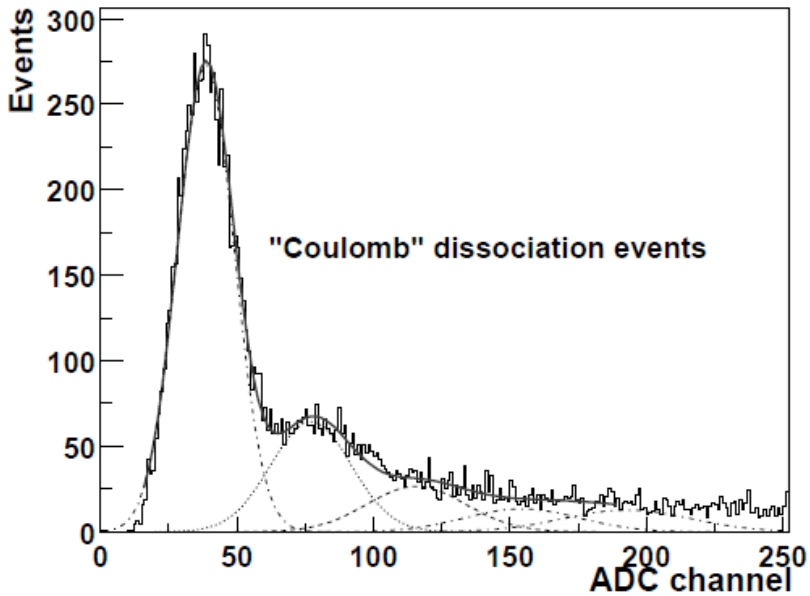

Figure 1.2: ZDC neutron spectrum at RHIC with each a Gaussian fit to the 1, 2, 3, 5, and 5 neutron peak [**?**].

Nuclear collisions were separated from photon-induced break up by counting hits in the central scintillating counter similar to a tracker. Events with hits on both sides of the interaction point were categorized as nuclear interactions, and those with no hits or hits on only one side were categorized as electromagnetic interactions. The difference in the charge measured on each of the two sides of the interaction point, by the two ZDCs, is divided by the total charge for both ZDCs (see Fig. **??**). Figure **??** shows that events created by electromagnetic interactions result in asymmetric neutron emission, whereas nuclear interactions produce neutrons on both sides. In the analysis presented in this thesis, the energy asymmetry in the ZDCs is used to select UPC events. This will be discussed in Chapter **????**.

Both the ρ^0 and J/ψ meson photoproduction cross sections in UPC events were measured at RHIC. STAR measured the photoproduction of the ρ^0 meson at collisions energies per nucleon of 62.4 GeV [**?**], 130 GeV [**?**], and 200 GeV [**?**]. The J/ψ was measured by PHENIX at 200 GeV [**?**]. The ρ measurements by STAR were in good agreement with the theory calculation method described in Section **??**. The J/ψ measurement where limited by statistic as only 10 J/ψ candidates were found.

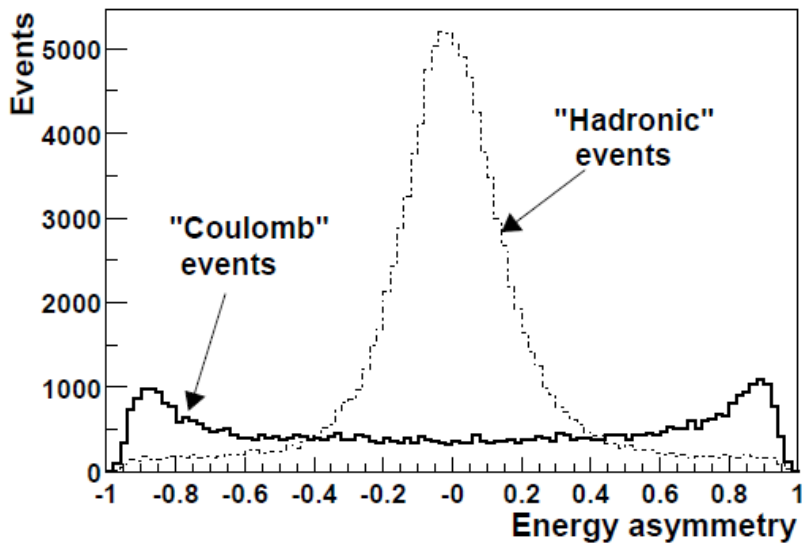

Figure 1.3: The energy asymmetry in the ZDCs for photon-induced interaction, coulomb events, and nuclear interaction, hadronic events [**?**].

1.6.2 UPC J/ψ at the LHC

The increase in beam energy from 200 GeV at RHIC to 2.76 TeV at the LHC results in an increase in the Lorentz γ of about 10. Because the photon flux depends on γ^2, the photon flux at the LHC increases by a factor of about 100 compared to RHIC. All major heavy ion experiments, ALICE and CMS, have studied the production of UPC events. ALICE has studied coherent J/ψ photoproduction in ultra-peripheral PbPb collisions at $\sqrt{s_{NN}}$ = 2.76 TeV. The cross section for this process was measured at both forward-rapidity, y = 3, and mid-rapidity, y = 0. With an integrated luminosity of 55 μb^{-1}, ALICE measured 78 $\pm$ 10(stat) $^{+7}_{-11}$(syst) coherent J/ψ candidates at forward rapidity. The measured cross section was 1.00 $\pm$ 0.18(stat) $^{+0.24}_{-0.26}$ (syst) mb. For a symmetric system like PbPb collisions, as opposed to pPb collisions, there is an ambiguity between which ion is the target and which is the photon emitter. Therefore, the cross section has a contribution from the low-x and high-x parts of the gluon density. At y = 3 for PbPb collisions at the LHC, the cross section has a contribution from both $x = 5 \times 10^{-5}$ and $x = 2 \times 10^{-2}$. This ambiguity is not present at y = 0. ALICE has also measured the coherent J/ψ photoproduction cross section at y = 0, using a integrated luminosity of about 23 μb^{-1}. 291 $\pm$ 18 (stat)$\pm$ 4(syst) and 265 $\pm$ 40 (stat)$\pm$ 12(syst)

coherent J/ψ candidates were measured in the dimuon and dielectron channels, respectively. The combined cross section from both channels was measured to be 2.38 $^{+0.34}_{-0.24}$ (stat+syst) mb. At y = 0 $x \sim 10^{-3}$, which is a smaller x than at forward rapidity, and more sensitive to the nuclear gluon shadowing (see Fig. **??**).

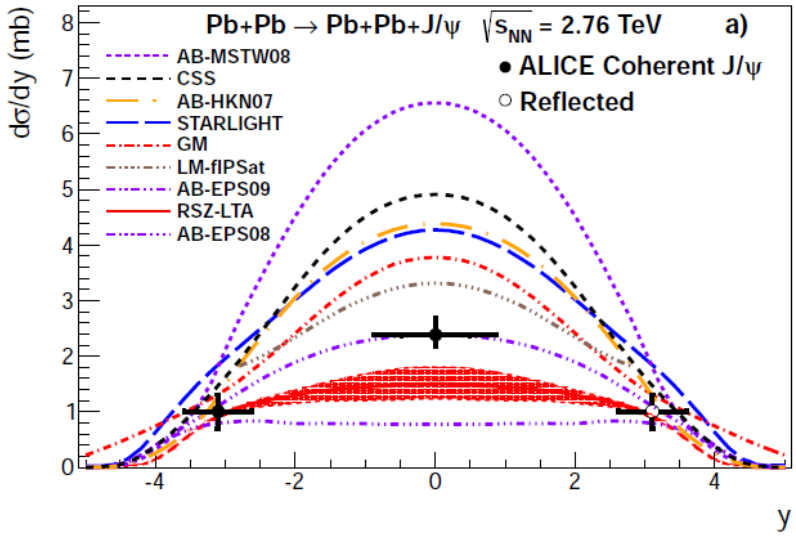

Figure 1.4: Coherent J/ψ photoproduction cross section in ultra-peripheral PbPb collisions at $\sqrt{s_{NN}}$ = 2.76 TeV, measured by the ALICE experiment at forward and mid-rapidity [].

The ALICE data points have been compared to several theoretical models. The UPC photoproduction cross section calculations depend significantly on how the nucleus is represented in the calculation. The results from the STARlight, LTA, and AB methods vary from a relatively large cross section in the STARlight model, ranging through a variety of values in the AB method, to a relatively small cross section in the LTA method. Each of these methods utilizes the same probe of the nucleus, the equivalent photon flux that is calculated using the Weizsäcker-Williams approximation (see Section **??**). The three methods deviate in how they calculate the forward photoproduction scattering cross section. The differences in the UPC photoproduction cross sections predicted by the different models demonstrates the amount of experimental sensitivity there is to distinguishing between the models. The dependence of the cross section on rapidity is clearly visible.

The cross section value calculated by Eq. **??** in the STARlight, LTA, and the various gluon

Model	$\sigma_{AA\to AAJ/\psi}(mb)$
STARlight/STARlight MC	23
LTA	9
AB-MSTW08	34
AB-EPS08	7
AB-EPS09	14
AB-HKN07	23

Table 1.1: $\sigma_{AA\to AAJ/\psi}(mb)$ the LTA, STARlight, AB methods. Four different gluon density models are used in the AB method. STARlight is a simulation software package that utilizes the STARlight model.

density models in AB method vary significantly. Table **??** gives the predicted values for the three main methods taken from [**?**], [**?**], and [**?**]. The cross sections in Table **??** differ by a factor of 4 from the smallest to largest and create an experimental opportunity. The clear discrepancy between the models in Table **??** demonstrates the high amount of experimental sensitivity there is for distinguishing between the models.

The nuclear suppression factor, S, demonstrates the difference between how the models represent the nucleus. S is the ratio between the nuclear photoproduction cross section and the free nucleon photoproduction cross seciton. It is a measure of how the nuclear gluon densities evolve in each of the models. Figure. **??** from [**?**] shows the nuclear suppression, which is equivalent to R_g in Eq. **??**, for the LTA and AB methods. Fig. **??** shows the nuclear suppression for the STARlight method [**?**]. Fig. **??** and Fig. **??** show that as the momentum of the probing photon goes up, increasing $W_{\gamma p}$, and momentum of the probed gluon goes down, decreasing x, the nuclear gluon density decreases relative to the free nucleon. The nuclear suppression factor, S, allows for the different models' representations of the gluon content of the nucleus to be directly compared to each other and to data. S can be measured from data by assuming a Weizsäcker-Williams photon flux and provides insight into nuclear gluon densities.

In addition, ALICE reported the measurement of the incoherent J/ψ photoproduction cross section at mid-rapidity. This provided additional constraints to the models for gluon shadowing.

In Chapter 1, the coherent UPC J/ψ photoproduction cross section using CMS is described.

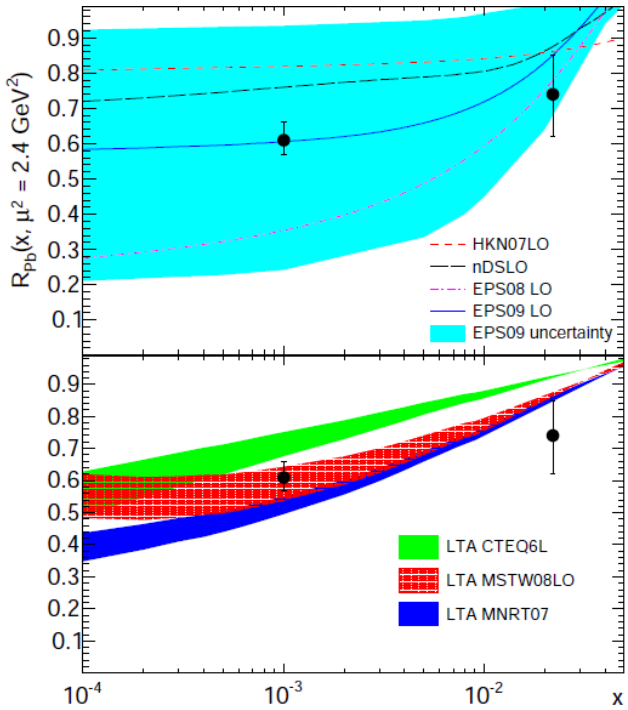

Figure 1.5: Nuclear supression factor, S, in the AB and LTA methods.

The measurement in this thesis adds to existing ALICE results, covering an intermediate range of x values.

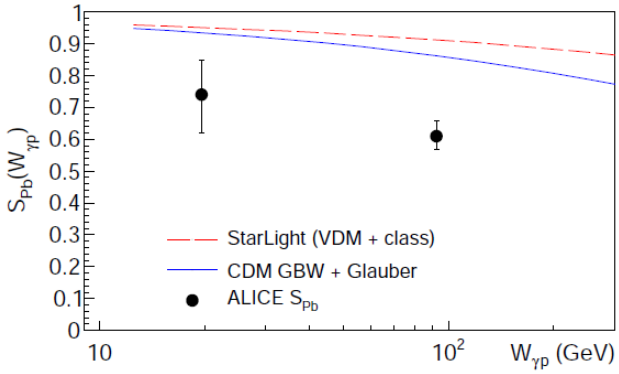

Figure 1.6: Nuclear supression factor, S, in STARlight method.

Chapter 2

UPC Trigger development for CMS

Rare physics process at the LHC require dedicated triggers in order to sort these processes from the billions of ordinary nucleus-nucleus collisions. Unlike most heavy-ion triggers, UPC triggers are optimized for low-p_T and low multiplicity events. For this reason trigger development specific to UPC events was required to carry out the analysis in this thesis.

The increase in collision rate of the LHC PbPb beams from 2010 to 2011 was nearly a factor of 15. To accommodate this increase in rate, the 2011 trigger scheme needed to be more selective than in 2010 where CMS could take any event which appeared to have a collision. The available bandwidth was allocated equally amongst the various heavy ion analysis groups to pursue as wide a physics program as possible. From this consideration, bandwidth limits were placed on the trigger rates for each analysis group's trigger package.

2.1 L1 trigger

The UPC L1 triggers were designed to study UPC J/ψ production via the dimuon and dielectron channels (see Section **??**). To achieve this, the loosest muon and electron triggers where combined with a trigger on energy in the ZDCs and no activity in BSCs (BSC veto). Additional triggers were commissioned in case radiation damage during the run reduced the sensitivity of the BSCs. This required no activity in HF (HF veto). These triggers are summarized in Table 1.1. The ECAL2

and ECAL5 triggers in Table 1.1 indicate a 5 and 2 GeV threshold on E_T measured in the ECAL. The MuonOpen trigger indicates that the trigger only requires a muon candidate in one of the three muon sub-systems and that there is no momentum threshold. ZDC in the trigger names indicate energy constant with at least one neutron. The sign on the ZDC label indicates which of the two ZDCs is required.

L1 trigger name	Rate (Hz)	Prescale	Id	Type
MuonOpen and (ZDC^+ or ZDC^-) and BSC veto	2.1	1	1	Physics
ECAL2 and (ZDC^+ or ZDC^-) and BSC veto	1.8	2	2	
ECAL5 and (ZDC^+ or ZDC^-) and BSC veto	0.3	1	3	
(ZDC^+ or ZDC^-)	35	1500	4	Monitor
MuonOpen and (ZDC^+ or ZDC^-) and HF veto	0	off	5	Backup
ECAL2 and (ZDC^+ or ZDC^-) and HF veto	0	off	6	
ECAL5 and (ZDC^+ or ZDC^-) and HF veto	0	off	7	

Table 2.1: List of 2011 L1 seeds.

The cumulative L1 trigger rate for all the UPC L1 trigger seeds was required to be no greater than 200 Hz. This requirement comes from the need to keep the tracker read-out rate low. The trackers baseline voltage can fluctuate due to the high tracker hit multiplicities in PbPb collisions. In order to monitor the zero suppression of the tracker, the zero suppression algorithm was executed using the HLT computing farm rather than in the tracker firmware.

In order to record the efficiency monitoring data, the ZDC triggers were reduce to a lower rate by only keeping a fraction of the total trigger rate. The factor that the trigger rate is reduced by is called the prescale. A prescale of 2 for example means that half the triggers that were accepted. If the prescale is set to 1, then whole trigger rate is accepted. The prescales for the triggers were set to balance the competing objectives of rate reduction and increasing the overlap between the monitoring and signal triggers.

2.2 HLT trigger

An event must pass the selection criteria of an HLT path in order to be recorded. As opposed to the

L1 trigger, which has access only to information from calorimeters and muon chambers, the HLT has access to all of the CMS sub-detectors including the tracker. Reconstruction of a track in the pixel detector is used by the UPC trigger paths. The use of the pixel detector only, as opposed to using the whole tracker including the silicon strip detector, allows for quick track reconstruction saving computing cycles. The UPC triggers were required to have at lease one reconstructed pixel track in order to reject backgrounds where no particles are reconstructed by the tracker. For the muon trigger in Table 1.2 the rate was reduced by nearly a factor or 4 compared to its L1 seed rate in Table 1.1.

HLT trigger	Rate (Hz)	L1 prescale	HLT prescale	L1 seed	Type
L1UPCMuon and Pixel Track	0.52	1	1	1	Physics
L1UPCECAL2 and Pixel Track	1.65	2	1	2	
L1UPCECAL5 and Pixel Track	0.26	1	1	3	
L1ZDCOr	3.6	1500	11	4	Monitor
L1ZDCOr and Pixel Track	2.8	1500	1	4	
L1UPCMuonHFVeto and Pixel Track	0	off	off	5	Backup
L1UPCECAL2HFVeto and Pixel Track	0	off	off	6	
L1UPCECAL5HFVeto and Pixel Track	0	off	off	7	

Table 2.2: List of 2011 HLT trigger.

The total HLT output for the UPC trigger package was limited to 20 Hz. The limiting factor for the HLT rate was the amount of disk space given to this analysis. To meet the bandwidth requirements and collect a significant sample of data for estimating efficiencies, the prescales were balanced with the goal of achieving at least 5% statistical precision on the efficiency measurements. As an example of the balancing of the prescales, the HLT ZDC trigger that did not require a pixel track was given a additional prescale factor of 11 on the HLT. The ZDC path that also required a pixel track on the HLT, which used the same L1 seed, was only prescaled at the L1. The prescale of 11 was set to ensure that at least 1000 of the pixel track ZDC triggers overlapped with the ZDC L1 only triggers so that efficiency of the pixel track requirement in the trigger could be estimated from the tracks lost.

2.3 Trigger development for the LHC pPb Run

Specific UPC triggers were also developed for the pPb run in 2013. For this period of running a much higher total trigger rate was read out relative to 2011. The total rate allocated for UPC triggers at the L1 in 2013 was 5 kHz and 50 Hz at the HLT. This factor of 5 increase in HLT and factor of 25 in L1 bandwidth, allowed for a change in emphasis from the L1 to the HLT.

The basic strategy in 2013 was the same as in 2012, use the loosest available ECAL and muon L1 triggers to push to capture the lowest p_T electrons and muons possible and reject hadronic interactions. Because of the L1 bandwidth restrictions in 2011, both the ZDCs and the BCSs were used on the L1 to reduce rates. In 2013 only the muon and ECAL triggers were used on the L1 allowing for rejection of hadronic interactions through cuts on track multiplicity. In addition, a more sophisticated trigger using full dimuon reconstructed was developed to increase purity. The main advantage in this shift in strategy was a higher purity due to the increased sophistication of the reconstruction on the HLT. In addition, an increase in cross section of the underlying physics process was achieved by relaxing the neutron emission requirement.

The HLT triggers in 2013 rejected hadronic interactions through counting tracks. For the five UPC trigger paths included in the HLT menu, three levels of reconstruction were done at the HLT.

- Pixel tracks were reconstructed from the inner pixel section of the silicone tracker alone, tracks were reconstructed using the full tracker using the strips as well, and full dimuon reconstruction was done using the tracker and muon detector.
- The least restrictive pixel track paths required at least one track reconstructed from the pixel detector and less than 10 pixel tracks in the event.
- Full tracking paths were added on top of the pixel track paths and included an additional requirement of one full track and less than 7 reconstructed tracks.
- The most restrictive path added to the pixel and full tracking paths and required reconstruction of dimuons with a mass between 2 and 12 GeV.

Chapter 3

Analysis

In this chapter the various parts of the analysis are explained. In Section 1.1, the simulations used to estimate the detector's ability to measure UPC processes are discussed. ~~Section 1.2 explains the considerations that went into the triggers that were developed for this measurement.~~ The selection of UPC events is detailed in Section 1.3. Extraction of the number of coherent J/ψ candidates is explained in Section 1.5. The determination of the detector's efficiency for measuring UPC events is explained in Section 1.6. Finally, Section 1.7 lays out the systematic uncertainties for the measurement.

3.1 Physics generators and Monte Carlo simulations

Every physical measurement is the product of the underlying physics folded with the response of the detector used to do the measurement. In order to understand the underlying physical process, the detector's effect on the measurement must be understood and accounted for. As instruments become more and more complicated, the interplay among all of the many parts of the detector makes an analytic approach to the problem untenable. For this reason, the numerical technique of Monte Carlo (MC) simulation is often the most effective approach for describing detector effects.

MC simulations use random number generation to model the many statistical effects of particles interacting with different parts of the detector. First, particles are generated according to theoretical

distributions. These particles are then propagated through a simulation of the detector. As the particles pass through the detector, random numbers are used to determine how these particles interact with the materials of the detector based on the known properties of the material. In this way, the theoretical distributions are convolved with a realistic model of the detector's response. A more detailed picture of how the detector shapes the underlaying distributions emerges with each successive event. The final goal of the MC simulation is to produce a set of events that accurately reproduce what would be measured if the theoretical input describes nature well.

3.1.1 STARlight and particle gun MC in CMS

In this thesis, two classes of generator input samples were used, STARlight [?, ?] and a particle gun. The STARlight samples ~~corresponds~~ correspond to the theoretical calculations described in Section **??**, while the particle gun produces particles with a user defined ~~momentum distribution~~transverse momentum distribution and rapidity distribution and isotropic decay to muon pairs in the J/ψ rest frame. For STARlight, three different physical process ~~are simulated;~~ were simulated: coherent J/ψ production, where the photon couples to the nucleus as a whole~~,~~ ; incoherent J/ψ production~~,~~ ; where the photon couples to a single nucleon within the nucleus, and photon-photon interactions, where the photons from the two nuclei interact with each other to produce a pair of oppositely charge muons~~directly~~. All three STARlight samples contain a μ^+ and μ^- in the final state. ~~The second class simulates particles with a user defined and rapidity distribution and isotropic decay to muon pairs in the rest frame.~~

Because STARlight is not integrated into the standard CMS software framework (CMSSW) [?] , a simulation software chain with 5 steps was developed. First, STARlight is run in the specified mode, and a single file is created for each physics process. In step 2, the STARlight output file is converted to the Les Houches (LHE) format [**?**], and the momentum of the parent J/ψ or the initial photon-photon pair is added to the record of each event. The event record produced by STARlight only contains the final state particles. To process the events in parallel, the STARlight files are subdivided in step 2, creating several LHE files from a single STARlight file. The LHE

files are used as input to CMSSW.

Steps 3 to 5 take place within CMSSW. In step three the generated particles are propagated through the GEANT4 [**?**] detector simulation. This accounts for all the interactions with the detector and produces as output a format identical to the raw data that is recorded during data taking. Steps 4 and 5 are processed using the same software as in data taking. In step 4 the reconstruction software used during data taking is run on the output of the detector simulation. The output of the reconstruction is reduced to the information that is needed for the final analysis in the final step.

The particle gun samples were created entirely within CMSSW. J/ψ mesons were created according to user defined p_T and rapidity distributions. The decay of J/ψs to ~~μ^+ and μ^-~~ a $\mu^+\mu^-$ pair was simulated with a ~~a~~ uniform decay distribution, corresponding to unpolarized J/ψ particles. As with the STARlight samples, these muons are propagated through the GEANT4 simulation [**?**] of the detector, and the raw data is produced. The remaining steps of running the reconstruction code and reducing the data to the final data format needed for the analysis are identical to the STARlight production.

The momentum of the final state muons is the main ~~drivers~~ driver of whether the candidate can be measured. One of the two ~~daughters~~ daughter muons must have large enough momentum to fire the trigger, and both muons must have enough momentum to be reconstructed and tagged as a muon. There are at least 10 ~~interactions~~ interaction lengths of material through which the muons must travel in order reach the muon chambers (see Fig.of about 7 GeV in order for muons can fire the trigger~~and be reconstructed~~.

The p_T distribution and the polarization of the J/ψs produced are the main factors controlling the momentum of the muon daughters, which vary for the different MC samples. The polarization effects how the momentum is shared between the daughters [**?**]. In the rest frame of the parent J/ψ, equal momentum is given to each daughter muon. However in the lab frame of the detector, the muon daughters which are emitted from transversely polarized J/ψ will tend to be emitted in the direction the J/ψ is traveling and will have unequal momentum in the lab frame. The daughter traveling in the direction of the J/ψ will have increased momentum, whereas the daughter traveling

opposite to the J/ψ direction will have decreased momentum.

In Fig. 1.1 the ~~of~~ J/ψs p_T from the STARlight generated coherent, and incoherent, and the dimuon p_T for photon-photon samples are compared. Both the coherent and the photon-photon samples are concentrated a low p_T, and neither sample extends much beyond 0.15 GeV. The incoherent sample is peaked near 0.5 GeV and extends beyond 1 GeV. The two particle gun samples resemble the incoherent and coherent samples p_T distributions. The first sample has a Gaussian p_T distribution extending to approximately 0.15 GeV, whereas the second is flat in p_T up to 2 GeV.

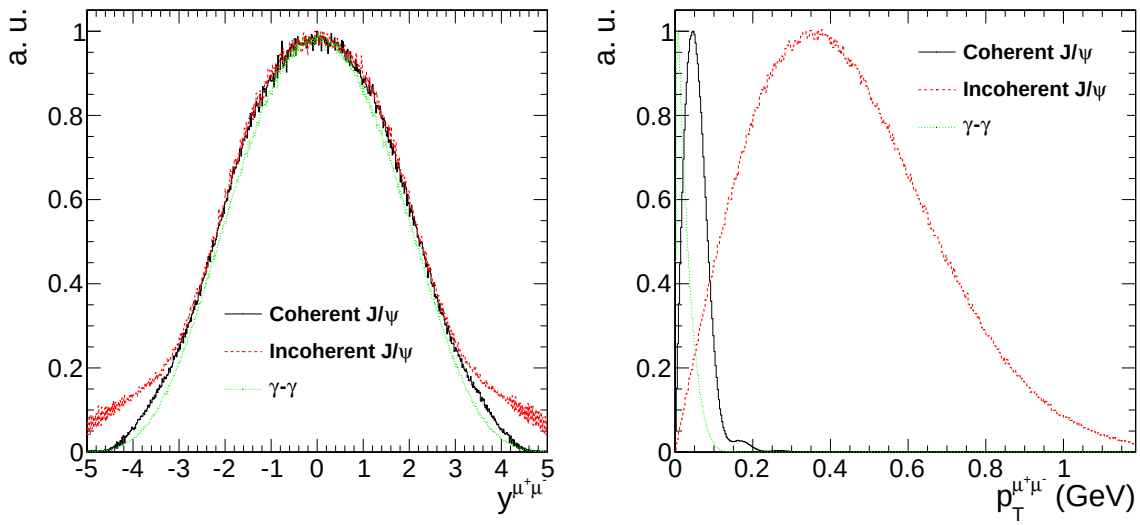

Figure 3.1: Generator level rapidity (left) and p_T (right) distributions for the coherent (black), incoherent (red), and photon-photon process (green).

The particle gun samples are unpolarized, whereas the STARlight samples have transverse polarization. In Fig. 1.2, the cosine of the helicity angle of the particle gun samples and the STARlight samples are shown. For the STARlight sample the helicity angle, the angle between the direction of the μ^+ daughter and the J/ψ direction in the rest frame of the J/ψ, prefer to be either parallel or anit-parallel. However, the particle gun samples have no preferred direction of emission.

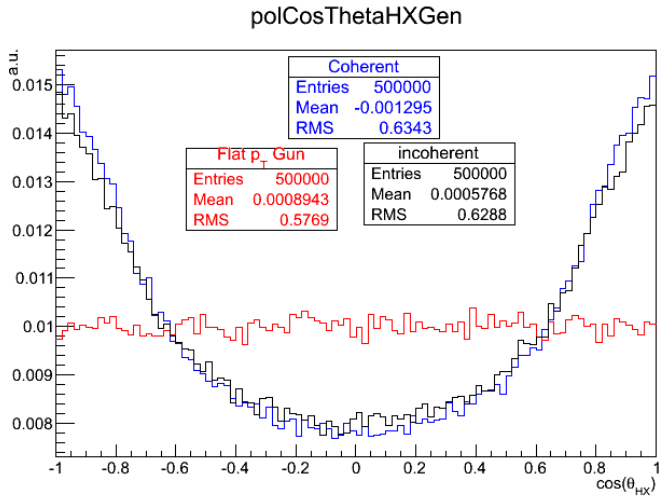

Figure 3.2: The J/ψ polarization of the particle gun (red), coherent (blue), and incoherent samples are plotted as the cosine of the helicity angle.

3.2 ~~Trigger development~~

~~A collection of triggers was needed in order to select UPC events from the collisions at the LHC. The increase in collision rate of the LHC PbPb beams from 2010 to 2011 was nearly a factor of 15. To accommodate this increase in rate, the 2011 trigger scheme needed to be more selective than in 2010 where CMS could take any event which appeared to have a collision. The available bandwidth was allocated equally amongst the various heavy ion analysis groups to pursue as wide a physics program as possible. From this consideration, bandwidth limits were placed on the trigger rates for each analysis group's trigger package. To ensure that UPC physics could be explored all while respecting the goals of the CMS Heavy Ions group as a whole, a UPC triggers were commissioned.~~

~~The UPC trigger rate estimates for commissioning the 2011 triggers were calculated by combining existing triggers from the 2010 run. By calculating the ratio between the UPC trigger rates and the minimum bias trigger rate, the UPC trigger rates were scaled up to the anticipated 2011 interaction rates using the 2010 data. The trigger package for 2011 contained ZDC based efficiency monitoring triggers, muon and electron based triggers for measuring , and backup triggers in case there was a problem with the original muon and electron triggers.~~

3.1.1 ~~L1 trigger~~

~~The UPC L1 triggers were designed to record enough data to measure UPC production via the dimuon and dielectron channels. To achieve this, the loosest muon and electron triggers where paired with a trigger on energy in the ZDC were used as a trigger selection criteria, and energy in the BSCs was used as a rejection criteria. Additional triggers with rejection criteria based on energy in HF were commissioned in case radiation damage during the run reduced the sensitivity of the BSCs. These triggers are summarized in Table 1.1. The 5 and 2 in the ECAL trigger names in Table 1.1 indicate a 5 and 2 GeV threshold on E_T measured in the ECAL. The Open in the muon trigger indicates that the trigger only requires a muon candidate in one of the three muon sub-systems and that there is not momentum threshold.~~

~~L1 trigger Rate (Hz) Prescale Id Type MuonOpen and (ZDC$^+$ or ZDC$^-$) and BSC veto 2.1 1 1 ECAL2 and (ZDC$^+$ or ZDC$^-$) and BSC veto 1.8 2 2 ECAL5 and (ZDC$^+$ or ZDC$^-$) and BSC veto 0.3 1 3 (ZDC$^+$ or ZDC$^-$) 35 1500 4 Monitor MuonOpen and (ZDC$^+$ or ZDC$^-$) and HF veto 0 off 5 ECAL2 and (ZDC$^+$ or ZDC$^-$) and HF veto 0 off 6 ECAL5 and (ZDC$^+$ or ZDC$^-$) and HF veto 0 off 7 List of 2011 L1 seeds. The cumulative L1 trigger rate for all the UPC L1 trigger seeds was required to be no greater than 200 Hz. This requirement stemmed from the need to keep the tracker read-out rate low. The trackers baseline voltage can fluctuate due to the high tracker hit multiplicities in PbPb collisions. In order to monitor the zero suppression of the tracker, the zero suppression algorithm was executed using the HLT computing farm rather than in the tracker firmware.~~

~~In order to record the efficiency monitoring data, the ZDC triggers had to be prescaled to a lower rate. The scaling down of the monitoring trigger was setup to ensure overlap with the signal triggers. The prescales for the triggers were set to balance the competing objectives of rate reduction and increasing the overlap between the monitoring and signal triggers.~~

3.1.1 ~~HLT trigger~~

~~An event must pass the selection criteria of an HLT path in order to be recorded. As opposed~~

~~to the L1 trigger, which has access only to information from calorimeters and muon chambers, the HLT has access to all of the CMS sub-detectors including the tracker. Reconstruction of a track in the pixel detector is used by the UPC trigger paths. The use of the pixel detector only, as opposed to using the whole tracker including the silicon strip detector, allows for quick track reconstruction saving computing cycles. The requirement of at least one reconstructed pixel track for the HLT triggers was designed to reject backgrounds where no particles are reconstructed by the tracker. For the muon trigger in Table 1.2 the rate was reduced by nearly a factor or 4 compared to its L1 seed rate in Table 1.1. This is due to the additional pixel track requirement. HLT trigger Rate (Hz) L1 prescale HLT prescale L1 seed Type L1UPCMuon and Pixel Track 0.52 1 1 1 L1UPCECAL2 and Pixel Track 1.65 2 1 2 L1UPCECAL5 and Pixel Track 0.26 1 1 3 L1ZDCOr 3.6 1500 11 4 L1ZDCOr and Pixel Track 2.8 1500 1 4 L1UPCMuonHFVeto and Pixel Track 0 off off 5 L1UPCECAL2HFVeto and Pixel Track 0 off off 6 L1UPCECAL5HFVeto and Pixel Track 0 off off 7 List of 2011 HLT trigger.~~

~~The total HLT output for the UPC trigger package was limited to 20 Hz. The limiting factor for the HLT rate was the amount of disk space available to store the data. To meet the bandwidth requirements and collect a significant sample of data for estimating efficiencies, the prescales were balanced with the goal of achieving at least 5% statistical precision on the efficiency estimates. As an example of the balancing of the prescales, the ZDC trigger that was passed through from the L1 was given a additional prescale factor of 11 on the HLT. The ZDC path that also required a pixel track on the HLT, which used the same L1 seed, was only prescaled at the L1. The prescale of 11 was set to ensure that at least 1000 of the pixel track ZDC triggers overlapped with the ZDC L1 only triggers so that efficiency of the pixel track requirement in the trigger could be estimated from the tracks lost.~~

3.2 Event selection

μb^{-1} **3.2.1Data sets** The unprecedented amounts of data produced by the LHC has made it possible to investigate novel physics processes like UPC J/ψ production. The data for this analysis were recorded during the 2011 LHC PbPb run. During this period, 150 μb^{-1} $\mu * 0b^{-1}$ were recorded by the CMS detector, corresponding to over a billion PbPb collisions. Of this, 143

The data were dived into three specially selected samples, Physics, Monitoring, and Zero bias, based on the triggers which recored the events (see Table **??**). This imposes an effective momentum threshold on v The J/ψ events discussed in this thesis were obtained analyzing the sample labeled in Table 1.3 as physics. A ZDC triggered monitoring sample was recorded for the sake of estimating efficiencies. Lastly, a zero bias sample was recored for investigating the ZDC and the noise distributions of HF.

The physics sample containing the J/ψ signal was recorded by the muon trigger labeled "L1UPCMuon and Pixel Track" in Table 1.2. Because of the characteristically low momentum of UPC J/ψ as compared to J/ψ created by other physics processes, the loosest muon trigger was used. The noise trigger rate for the muon trigger alone was 50Hz50 Hz, but in coincidence with the BCS veto and the ZDC trigger the noise rate was below 2Hz2 Hz. By pairing the muon trigger with the ZDC on the L1, the noise contribution was reduced from the noise contribution from either of the two sub-detectors to the noise coincidence between the two sub-detectors. Contributions from hadronic interactions are reduced by the veto on the BSCs. This trigger was designed to balance reducing the rate with maximizing the efficiency, allowing for the data to be recorded without producing high rates resulting that would have resulted in dead time for the detector.

In order to investigate the muon trigger and the other parts of the event selection, a monitoring sample was recorded by requiring energy consistent with at least one neutron in either of the ZDCs. Neutron production is a much more common process than the UPC J/ψ production. This process has cross sections on the order of 100 b compared to 10 mb predicted for J/ψ production. For this reason, the rates of this trigger are much higher than the physics trigger, and only a small sub set of these events are recorded. From this trigger the pixel track portion of the HLT trigger efficiency

Sample	Events	$\mathscr{L}_{int}$
Physics 1.1M	346K 31.6 mb^{-1}	143.3 ~~μb^{-1}~~ 1.3). By recording this hierarchy of samples, interesting events are select
Zero Bias	8.8M	580 b^{-1}

Table 3.1: Integrated luminosities and number of events for the three samples used in this analysis.

was estimated as well as the ZDC trigger efficiency, as will be described in Section 1.6.

In addition to the monitoring and physics sample, a zero bias sample was recorded to examine the ZDC neutron reconstruction and the HF noise distributions. The zero bias trigger fired every time both beams passed through CMS. Only 4 events out of every million triggered were recorded for this sample. This sample allowed for an unbiased measurement of the ZDC neutron threshold energies as discussed in Section 1.4. Because the zero bias trigger ~~does not require any activity in any of the CMS sub detectors~~only requires the presents of both LHC beams, the sample contains very few hadronic collisions. This allowed for a measurement of the electronic noise distribution in the HF, which are important to reducing contamination from hadronic interactions.

The integrated luminosity for each of the three samples is calculated by recording activity in HF ~~, the forward hadronic calorimeter in CMS~~ [**?**]. The cross section for HF activity is measured from a van der Meer scan~~, and the cross section was found to be 45 mb for proton-proton running~~. In this way, the amount of integrated luminosity for any running period is related to the activity in HF.

3.2.2 Event selection cuts

The analysis described in this thesis focuses on UPC J/ψs decaying to muons. The trigger used for this analysis recored 346841 events. A set of off-line cuts were applied to increase the relative contribution of UPC events to background processes. Two sets of event selection cuts were applied to reject background events. The first set rejects background from the beam. The second rejects events where hadronic collisions have occurred. Table 1.4 summarizes all the event selection cuts.

To reject beam induced background the following cuts were applied:

Cut type	Cut	Events
–	all triggered	346841
beam background rejection	good vertex requirement	340997
	beam halo muon rejection	302777
	cluster shape compatibility requirement	233590
hadronic interaction rejection	single-sided neutron requirement	149992
	two track requirement	32732
	HF signal rejection	5392
fake muon rejection	muon quality requirement	2047
kinematic cut	J/ψ mass requirement	696
	muon detectability cuts	567

Table 3.2: Effects of event selection cuts.

- The reconstructed vertex must be within 2 cm in the transverse direction and 25 cm in the longitudinal direction. This cut ensures that reconstructed particles come from interactions between the two beams rather than event where one of the two beams interact with gas particles near the interaction point.

- Beam halo muons were rejected using the timing of the muon hits. The beam halo cut rejects events where muons surrounding the beam stream through the detector.

- Pixel cluster shape should be compatible with the vertex. This cut requires that energy deposits in the silicon tracker point back to the reconstructed primary vertex.

These beam background cuts do not reject any UPC J/ψ candidates.

The second set of background rejection cuts were designed to reduce contamination from hadronic interactions.

- No more than 2 reconstructed tracks in the event. The track requirement rejects events that produce many charged particles.

- Maximum reconstructed hit energy in HF was required to be below the threshold for electronic noise. Nearly all hadronic interactions (about 98%) produce particles in the range $3 < |\eta| < 5$ covered by the HF detector. By requiring that the energy deposits in HF resemble noise, nearly all elastic hadronic collisions are expected to be rejected.

- Energy in the ZDCs consistent with neutrons on only one side of the interaction point. In hadronic interactions both nuclei break-up. By requiring that ZDC only reconstruct neutrons on one side of the interaction point, hadronic interactions that produce neutrons on both sides were rejected.

Each of these cuts were designed to reject topologies produced by hadronic interactions. The effect of these cuts can be seen in Table 1.4 and are denoted hadronic interaction rejection.

To establish the HF noise thresholds, the noise distributions were measured in zero bias events. An offline selection of events with no reconstructed tracks was used to ensure that no collision had taken place. The HF noise threshold was defined as the cut that keeps 99% of the zero bias events. The noise distribution from this zero bias sample is compared to the physics sample and MC in Fig. 1.3.

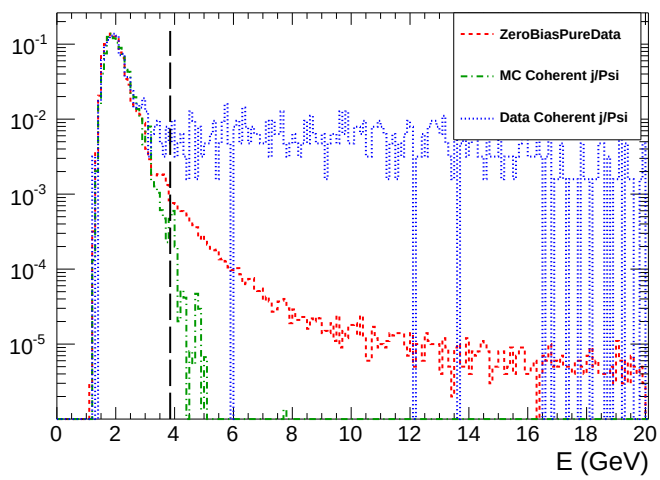

Figure 3.3: Comparison of HF noise distributions in zero bias data, physics triggered data, and MC.

The following standard muon quality cuts are applied:

- Tracker track matched with at least one muon segment (in any station) in both X and Y coordinates ($< 3\ \sigma$).

- Cut on number of tracker layers with hits > 5.

- Number of pixel layers > 0.
- The χ^2 per degrees of freedom of the track fit < 3.
- Loose transverse and longitudinal impact parameter cuts, ~~with in~~ within 3 cm in the transverse direction and ~~withing~~ within 30 cm in the longitudinal direction with respect to the primary vertex.

These cuts are applied to reduce the number of fake muons and have been validated for ~~standard muon analyses~~ other muon analyses [?] .

3.3 Break up determination

As described in Section **??**, UPC J/ψ photoproduction can be accompanied by the emission of neutrons from either of the two colliding nuclei. The various neutron emission scenarios, or break-up modes, can be distinguished by the two ZDCs. By separating events where the ZDC signal is consistent with 1 neutron versus several neutrons, or where neutrons are present on only one or both sides, the fraction of events which ~~correspond~~ corresponds to a given break-up mode can be measured and compared to theory.

In order to maximize the ability to explore the one neutron peak, which sits at the bottom of the ZDCs dynamic range, a new ZDC reconstruction method was devised. This new reconstruction method was then used to establish a one neutron and many neutron threshold. This section describes the ZDC signal reconstruction and how the neutron thresholds on this signal were set.

3.3.1 ZDC signal reconstruction

The signal from each ZDC is built up from the pulse shapes for each of the 18 individual ZDC channels. The pulse shape is recorded in 250 ns second chunks and is divided into 10 time slices of 25 ns (~~See~~ see Fig 1.4). Counting from 0, the 4th time slice is synced with the timing of the rest

of the detector and corresponds to when the products of the recorded collision reached the ZDC. The channel signal is therefore taken from the 4th time slice.

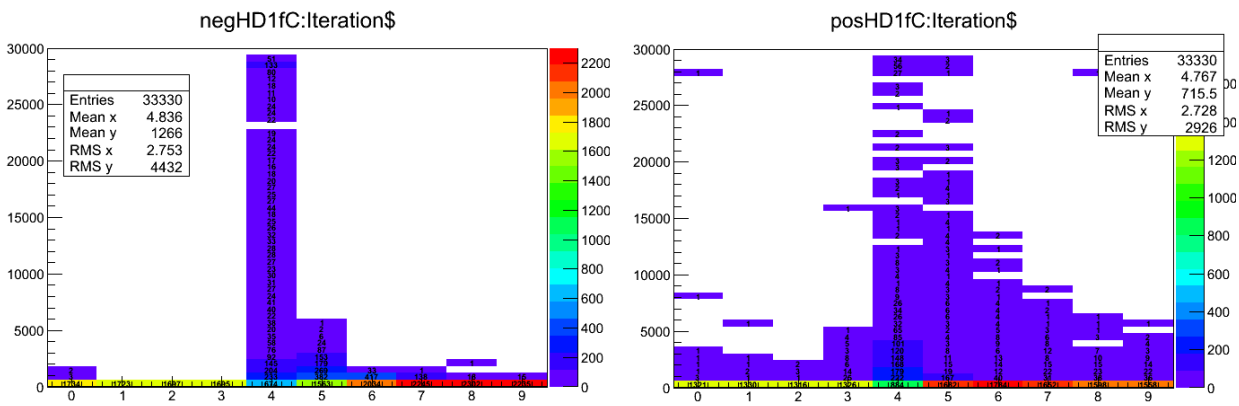

Figure 3.4: Average ZDC pluse shape is plotted as the charge as a function of time slice for the first hadronic from ZDC^{-} (left) and ZDC^{+} (right).

The ZDC signal sits on top of a low frequency noise pedestal with a period of about 2μ seconds. Over the time scale of 250 ns, this low frequency noise signal appears as a constant that shifts randomly from event to event. The contribution from this noise is therefore measured event by event in order to subtract it. Time slice 5 is used for this purpose. Time slices 1 and 2 could also be used to estimate the low frequency noise. However because the noise fluctuates to negative values of charge that cannot be measured, these time slices can only provide a measurement of the noise half the time. By using time slice 5 which contains the falling tail of the signal, the noise can be measured any time the signal raises significantly above the noise. If the fraction of signal in time slice 4 and 5 are constant and the noise contributes the same value to both time slices, the following formula is applicable:

$$Ts4 \propto (Ts4 + C) - (Ts5 + C) = Ts4 - R_{Ts5/Ts4} Ts4 = Ts4(1 - R_{Ts5/Ts4}), \tag{3.1}$$

where $Ts4$ is the signal contribution in time slice 4, $Ts5$ is the signal contribution to time slice 5, C is a random noise constant from the low frequency noise, and $R_{Ts5/Ts4}$ is the ratio between the signal contribution from time slice 5 over time slice 4. Figure 1.5 demonstrates the ~~consistence~~

consistency of the fraction and validates the unconventional method of using the falling tail of the signal to estimate the low frequency noise. By using time slice 5, the chances of measuring the noise are maximized. Separating the signal from the noise is especially important because the ZDC signal for the one neutron peak sits near the noise at the bottom of the ZDC dynamic range.

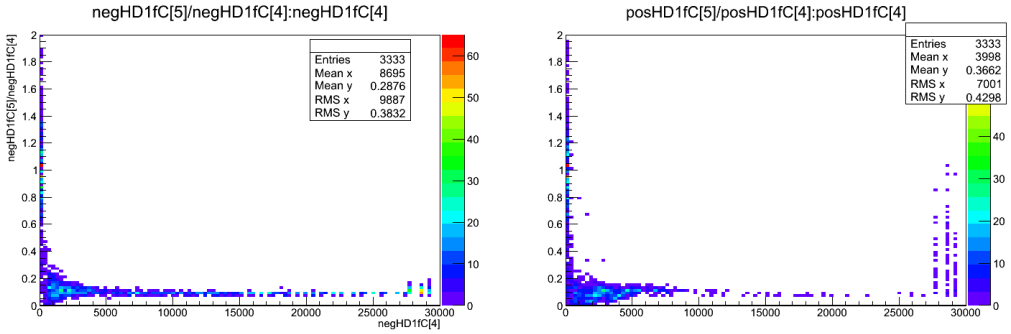

Figure 3.5: The fraction of signal in time slice 5 over time slice 4 as a function of the signal in time slice 5 in ZDC$^-$ (left) and ZDC$^+$ (right).

When summing the 9 channels in each ZDC only channels with signals above zero in time slices 4 and 5 were included. The EM, electromagnetic, section of the calorimeter is more densely packed with quartz fibers and therefore has a higher gain relative to the HAD, hadronic, section. To account for this, the EM channels were weighted with a factor of 0.1 to match the HAD channel gains.

3.3.2 Determination of the one neutron thresholds

The ZDC thresholds used to establish the various break-up modes were measured from zero bias data. Figure 1.6 shows the weighted sum of the EM and HAD sections for ZDC$^-$ and ZDC$^+$ for the zero bias dataset. The neutron spectrum for this dataset ~~does~~ is biased since the trigger only required that both beams were present in CMS. This does, however, include a significant electronic noise contribution due to events where no neutrons are emitted in the direction of the ZDC. It is clear from Fig. 1.6 that the gain of ZDC$^+$ is lower than that of ZDC$^-$. This is because of a damaged phototube on the first HAD section of ZDC$^+$.

To determine the thresholds for one and multiple neutrons, the ZDC$^+$ and ZDC$^-$ spectra were

fit. Four Gaussian functions were combined to fit the spectra. The electronic noise was fit to a Gaussian around zero. The one, two, and three neutron peaks are fit to Gaussians that are successively broader. The mean of each peak was initially set to multiples of the mean of the one neutron peak. The threshold for a neutron in the ZDC was taken from the fits in Fig. 1.6. Any signal greater

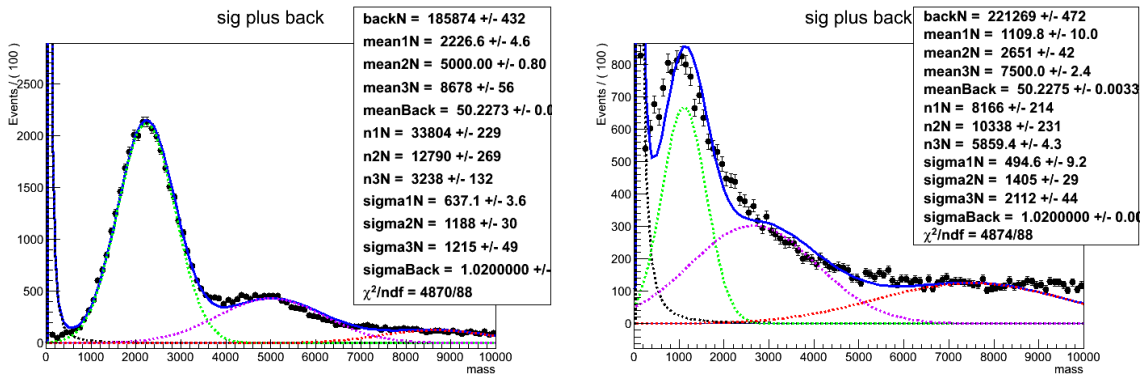

Figure 3.6: Fit to the signal spectra for ZDC^{-} (left) and ZDC^{+} (right)

2σ below the mean of the one neutron peak was considered signal. Any signal greater than 2σ above was considered multiple neutrons. The single neutron break up modes were separated from the multiple neutron modes by use of these definitions.

Several of the break-up mode calculations that have been done involve single sided configurations where neutrons are present on one side of the interaction point and not the other. These modes can be hard to identify because the single neutron peak in ZDC^{+} overlaps with the noise peak at zero. To identify events where the ZDCs only measured noise, the noise spectrum were measured directly. Placing an additional criteria based on the ZDCs noise distributions for when the ZDCs are devoid of signal provides assurance that the events tagged as single sided events are truly single sided.

The noise distributions for the EM sections and the HAD sections were measured separately from out of time time slices. In Fig. 1.4 higher than average signal can be seen in the 0th time slice, which precedes the main signal time slice time slice 4 by 200 ns. This is due to events where activity was present in the ZDC for two consecutive collisions. Time slices 1 and 2, however, occurred between collisions. These time slices, which occur out of time, were used to measure the

noise spectrum.

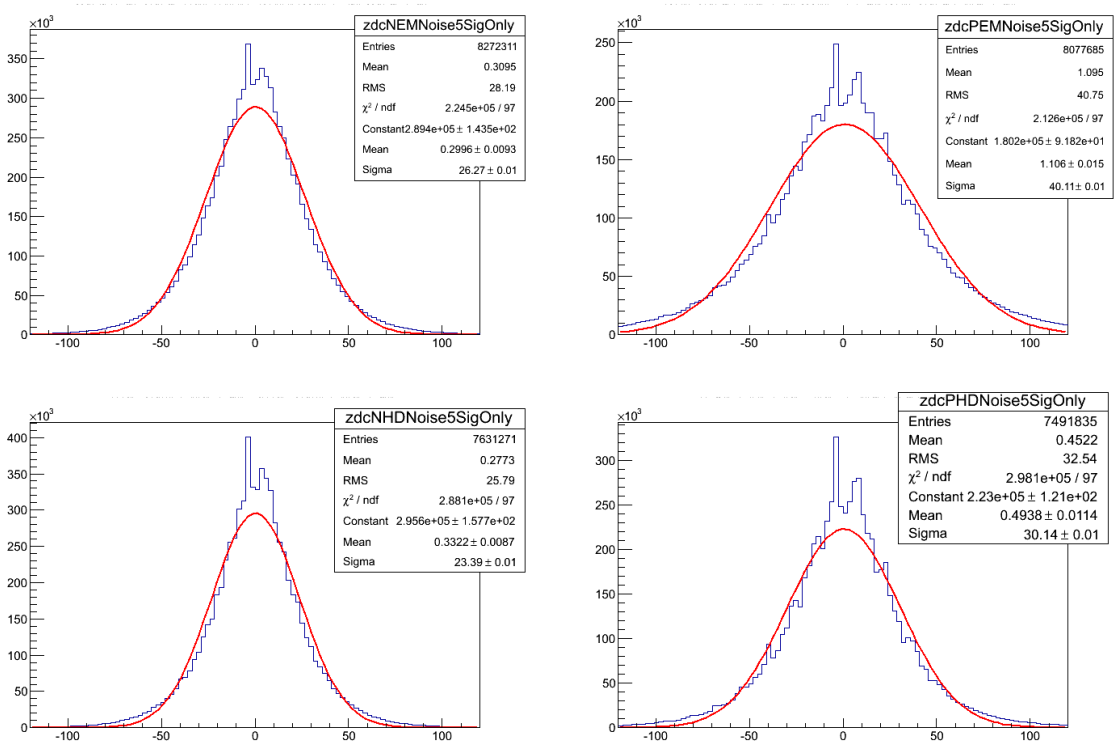

Figure 3.7: ZDC noise spectra from ZDC$^-$ EM section (upper left), ZDC$^+$ EM section (upper right), ZDC$^-$ HAD section (lower left), and ZDC$^+$ HAD section (lower right) from out of time time slices.

As with the signal measurements, the low frequency noise pedestal is subtracted event by event by subtracting time slice 2 from time slice 1 leaving only the high frequency noise. The noise distributions do not depend on the amount of quartz fibers, but because the signal does, the noise distributions for EM and HAD sections are measured separately. ~~Fig~~Figure 1.7 shows the noise spectrum for each of the EM and HAD sections for the two ZDCs. If the HAD or EM signals measured from time slices which match the timing for a collision, time slices 4 and 5, are less than 2σ above the mean of the noise distribution or lower, these sections are considered consistent with noise. A ZDC is considered consistent with noise if both the HAD section and EM section from that ZDC have signal measurements consistent with noise.

3.4 Signal extraction

After all event selection cuts, the remaining events contain a combination of coherent J/ψ, incoherent J/ψ, and dimuons from the photon-photon process. Each process must be separated from the final mix. To achieve this, the invariant mass and p_T distributions are used to distinguish between the three processes. The photon-photon process is extended in invariant mass whereas the J/ψ is peak strongly near 3.1 GeV. In dimuon transverse momentum distribution of the photon-photon and coherent process have similar distributions, both peaked shapely below 0.1 GeV, whereas the incoherent process is more broadly distributed across an interval extending to nearly 1 GeV. The mass distribution was fit to separate the photon-photon process from the J/ψ process. The p_T distribution was used to separate the incoherent process from the photon-photon process, and the coherent process. In this way, a separate yield was extracted for all three processes.

The invariant mass distribution for opposite sign dimuons is shown in Fig. 1.8. A J/ψ signal is clearly visible together with tails at higher and lower mass due to the photon-photon process. A fit to the invariant mass distribution was ~~done~~ performed using a Gaussian to account for the J/ψ signal and a ~~first order~~ first-order polynomial function for the photon-photon process. The extracted number of J/ψ candidates from this fit includes all J/ψs in the mass window that passed the analysis cuts, i.e. both coherent and incoherent process contribute to yield from the mass fit. The p_T distribution is needed to separate the two different contributions to the J/ψ peak.

Figure 1.9 shows the p_T spectrum of the events plotted in Fig. 1.8. There is a clear coherent peak at p_T = 60 MeV followed by broad distribution that peaks near p_T = 450 MeV. To extract the contribution of coherent, incoherent and gamma-gamma processes in the data the spectrum in Fig. 1.9 was fit to the sum of three MC templates corresponding to the final output of the MC simulations for these three processes. The clear overlap of the coherent and photon-photon process, and the clear separation of these two lower p_T processes from the incoherent process is apparent. The shape of the p_T distribution for the coherent, incoherent, and photon-photon process are taken from the final output of MC after applying all analysis cuts. In Fig.1.9, the yield parameters that were fit were left unconstrained for all three process.

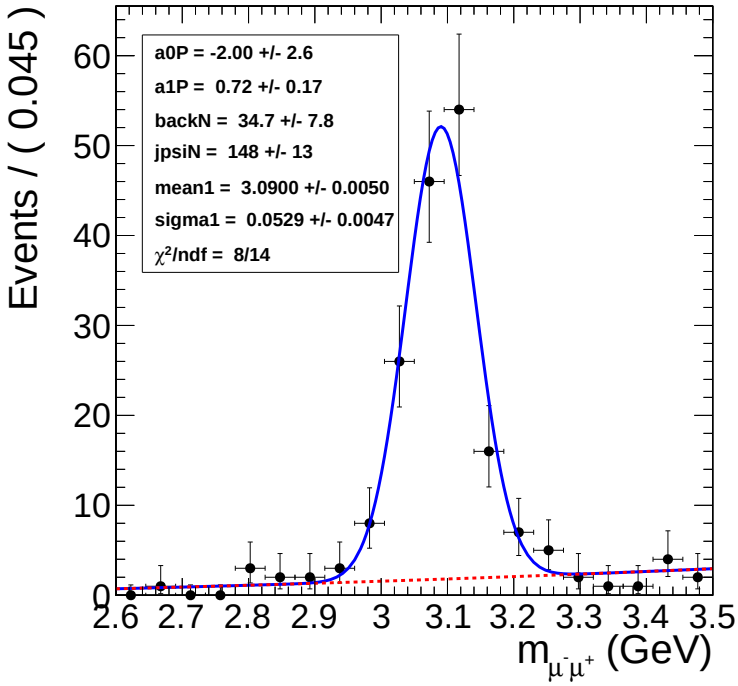

Figure 3.8: Mass fit to J/ψ using Gaussian for the signal and a ~~first order~~ first-order polynomial for the photon-photon continuum.

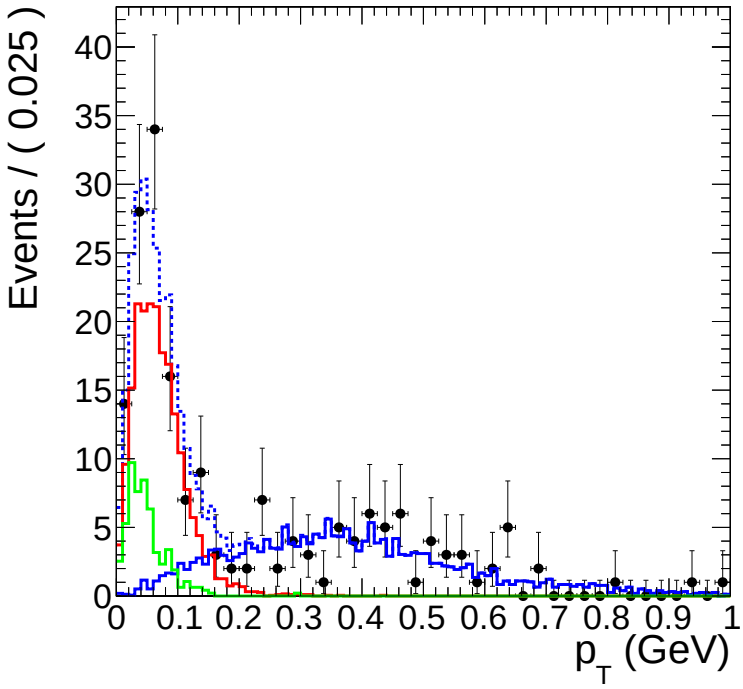

Figure 3.9: Fit to MC p_T templates.

The shape of the photon-photon and coherent J/ψ process are very similar in transverse momentum. Accordingly, the contribution from the photon-photon process and the coherent process are difficult to separate from the p_T distribution. The confidence contours in Fig. 1.10 from the template fit in Fig. 1.9 demonstrate the strong anti-correlation between the coherent yield parameter, *nCo*, and the yield parameter for the photon-photon process, *nGamma*. Because of the anti-correlation, the statistical uncertainty on *nCo* and *nGamma* from the fit are larger than $\sqrt{nCo}$ and $\sqrt{nGamma}$ expected from Poisson statistics. The information from the invariant mass and p_T distributions were combined to break this correlation. Through this combination, the contribution to the final yield from the three process was measured.

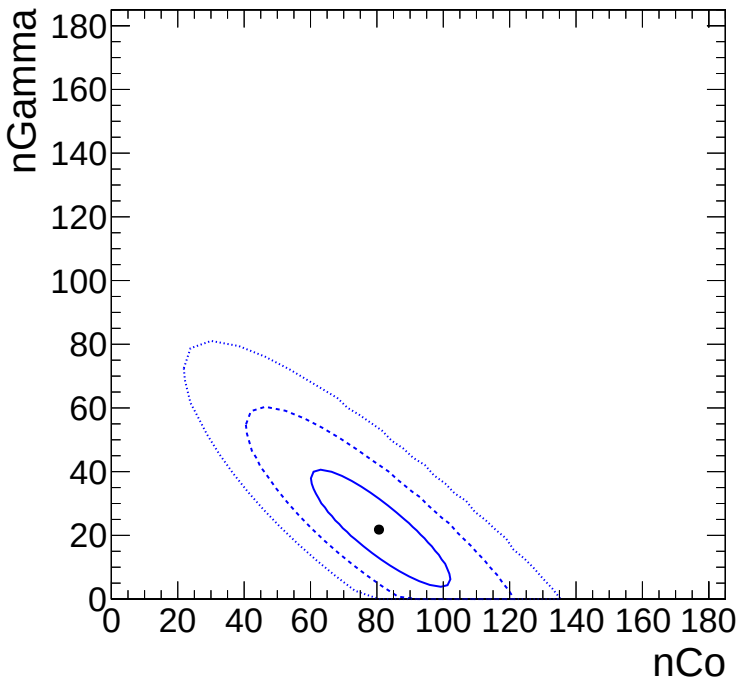

Figure 3.10: 68%, 95%, and 99% confidence contours from the p_T template fit.

A simultaneous fit to the mass spectrum and p_T spectrum was preformed to utilize the mass fits ability to distinguish the photon-photon process from the coherent and incoherent process all while utilizing the p_T fits ability to separate the coherent and photon-photon processes from the incoherent. Fig. 1.11 shows the result of the simultaneous fit. The simultaneous fit forces the parameter *nGamma* to both describe the photon-photon continuum present in the side bands of the

J/ψ mass peak as well the photon-photon contribution to the low-p_T part of the p_T spectrum. In addition, the J/ψ yield from the mass fit is forced to equal the contribution from the incoherent and coherent process in the fit to the p_T distribution. In this way, the correlation between the yield parameters was broken, and the contribution from the three process were made independent of each other.

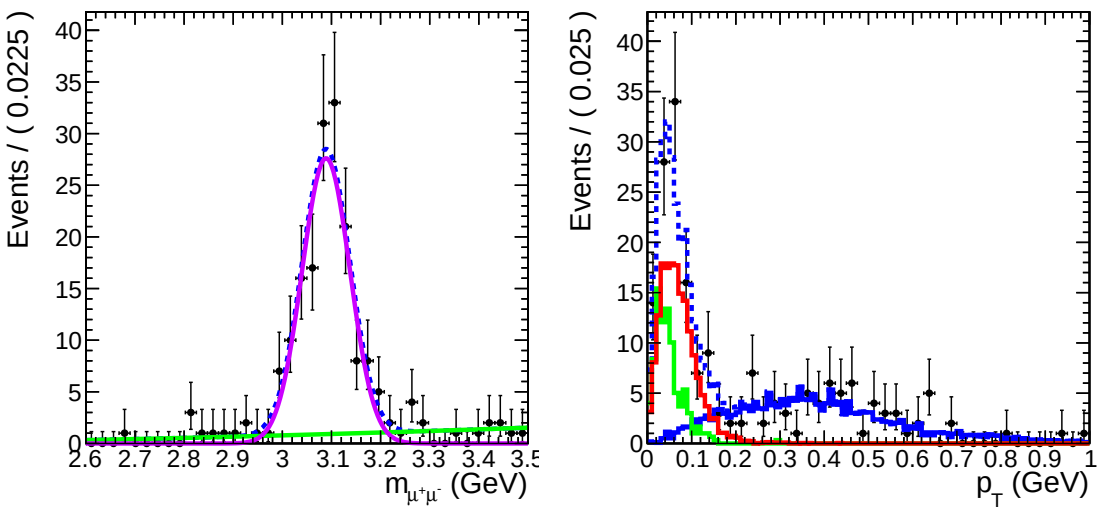

Figure 3.11: Simultaneous fit to the mass and p_T spectra.

Fig. 1.12 shows the confidence contours for *nCo* and *nGamma* from the simultaneous fit in Fig. 1.11. The slope of the confidence contours in Fig. 1.12 is noticeably than in Fig. 1.10. The contours for the simultaneous fit are also reduced compared to Fig. 1.10 with widths in *nCo* and *nGamma* similar to those expected from Poison statistics. From the simultaneous fit, reasonable statistical errors were obtained along with the yields for the three processes.

3.5 Efficiency determination

Each step of the triggering, event selection, and analysis has an associated efficiency that must be accounted for in the measurement of the J/ψ cross section. The ZDC trigger efficiency, the muon trigger efficiency, and the muon reconstruction efficiency are the two most significant contributors to the total efficiency measurement. The efficiency of the pixel track requirement, and the veto on

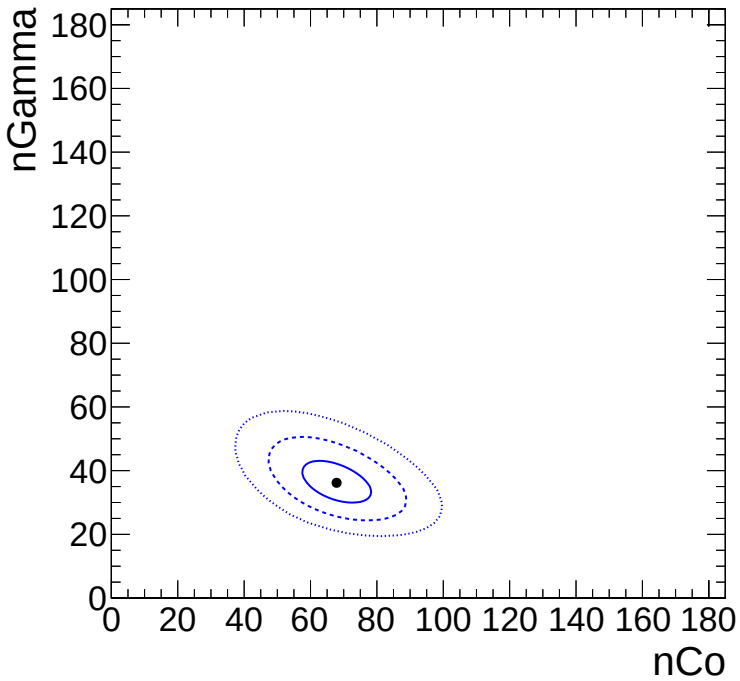

Figure 3.12: 68%, 95%, and 99% confidence contours from the simultaneous fit.

activity in the BSCs from the trigger are also estimated but found to be consistent with fully efficient. The following section explains how each of these efficiencies were measured with a special emphasis on the ZDC trigger efficiency and the muon trigger and reconstruction efficiencies.

3.5.1 Muon efficiencies

The muon efficiencies were measured using a combination of MC and data based methods. The MC based measurement accounts for the detector acceptance and the efficiency of the muon quality cuts discussed in Section 1.3. The trigger efficiencies were measured in data using the tag and probe method [**?**], which is discussed below.

CMS has a limited acceptance for J/ψs, particularly in the case of J/ψs with low momentum like those produced in UPC events. To measure the acceptance of CMS for J/ψs, reconstructed dimuon candidates were considered detectable if both reconstructed muon daughters fell into a detectability region in p_T and η. The muon detectability region was defined using the coherent J/ψ events obtained from STARlight. The efficiency for reconstructing single muons ε^{μ}_{reco} is defined by

$\varepsilon^{\mu}_{reco} = \frac{N^{\mu}_{reco}}{N^{\mu}_{gen}}$, where N^{μ}_{reco} is the number reconstructed muons obtained after the full CMS detector simulation and that passed the standard muon quality cuts, and N^{μ}_{gen} is the number of generated muons from STARlight. Fig. 1.13 shows the efficiency for reconstructing single muons from co-

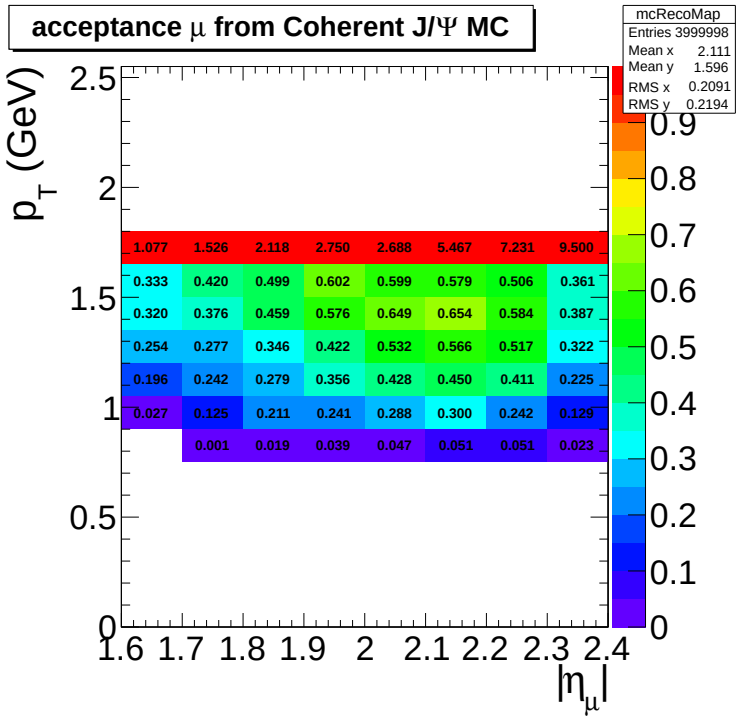

Figure 3.13: Muon daughter detectability from coherent J/ψ

herent J/ψ events. To avoid the edges of the detectors acceptance, all reconstructed muons that fall into a $(p_T, |\eta|)$ bin that has an efficiency less than 20% were rejected. This condition defines the detectability region. The acceptance for reconstructing dimuons was calculated from MC using the following formula:

$$A = \frac{N_{det}(|y|, p_T)}{N_{gen}(|y|, p_T)}, \tag{3.2}$$

where N_{det} is the number of reconstructed dimuons where both daughters fall into the detectability region, and N_{gen} is the number of generated dimuons. From Eq. 1.2, the acceptance for J/ψ was calculated as a function of $|y|$, and p_T (see Fig. 1.14).

The "tag and probe method" is a data driven approach used to measure the trigger efficiency of the muon daughters from J/ψ decays. In this method there are three categories of daughter muons.

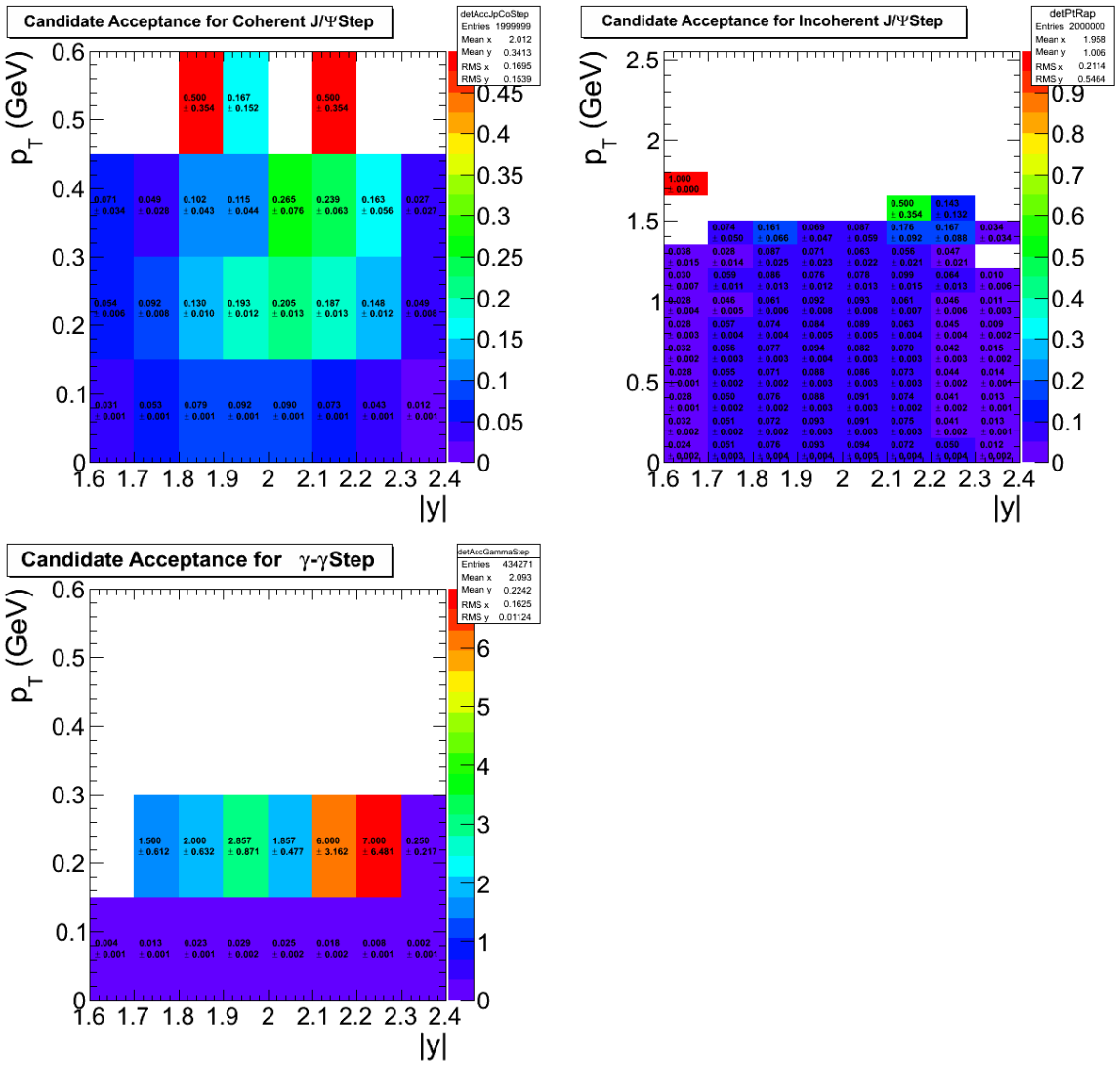

Figure 3.14: Dimuon acceptance from coherent J/ψ (top left), incoherent Jψ (top right), and photon-photon interactions (lower).

Tag muons are high quality muons. *Passing probes* are reconstructed muons that match the muon trigger, while *failing probes* do not. Each dimuon will have one daughter classified as a tag and the other as a probe. From here three invariant mass histograms are studied. One histogram is created from all pairs. The second comes from pairs where the probe is a passing probe. The last histogram comes from pairs where the probe fails to fulfill the trigger, ~~*i.e.* the probe~~ it is a failing probe. By matching the tag to the trigger, the probe is unbiased by the trigger and the efficiency can be measured by fitting the three mass histograms.

Because the trigger efficiency depends on the p_T and $|\eta|$ of the muon, one set of three histograms for each (p_T,$|\eta|$) bin of the probe is created. To extract the single muon trigger efficiency ε^{μ}_{trig}, each set of invariant mass histograms were simultaneously fit. The signal was ~~fitted~~ fit using a Crystal Ball function, and the background was ~~fitted~~ fit to an exponential. The Crystal Ball parameters were simultaneously ~~fitted~~ fit to all three histograms. The exponential function was ~~fitted~~ fit to the failing and passing probe histograms separately. Because the background shapes are in principle different for the two samples, the efficiency is driven by this difference.

Fig. 1.15 shows the fit of the three sets of pairs. This fit was done for each bin of the probes p_T

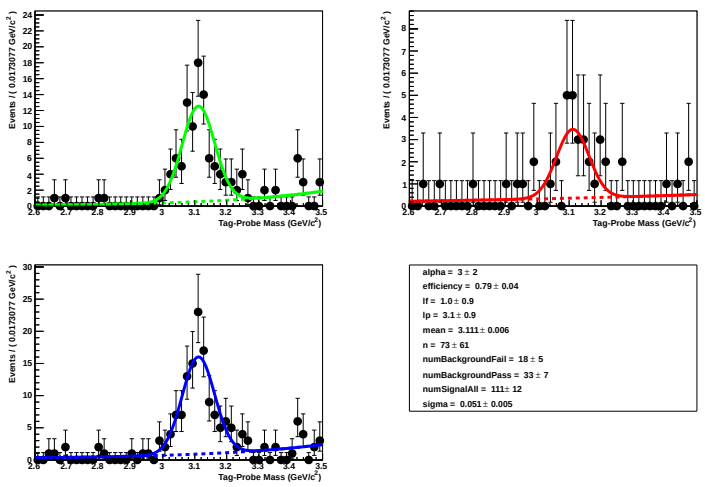

Figure 3.15: Fits to tag and probe pairs in the J/ψ mass region for pairs with a probe $2 < |\eta| < 2.2$ and $1.55 < p_T < 1.8$ GeV.

and η. The efficiency from the fits in each bin are shown in Fig. 1.16.

The dimuon trigger efficiency $\varepsilon^{dimuon}_{trigger}$ was calculated from the single muon efficiencies using the following equation:

$$\varepsilon^{dimuon}_{trigger} = 1 - (1 - \varepsilon^{\mu_1}_{trigger})(1 - \varepsilon^{\mu_2}_{trigger}), \tag{3.3}$$

where $\varepsilon^{\mu_1}_{trigger}$ is the tag and probe efficiency of the first dimuon daughter, and $\varepsilon^{\mu_2}_{trigger}$ is the efficiency of the second muon daughter. In Eq. 1.3 the probability of at least one daughter firing the trigger is calculated by subtracting one from the probability that neither daughter fires the trigger, thus giving the dimuon trigger efficiency.

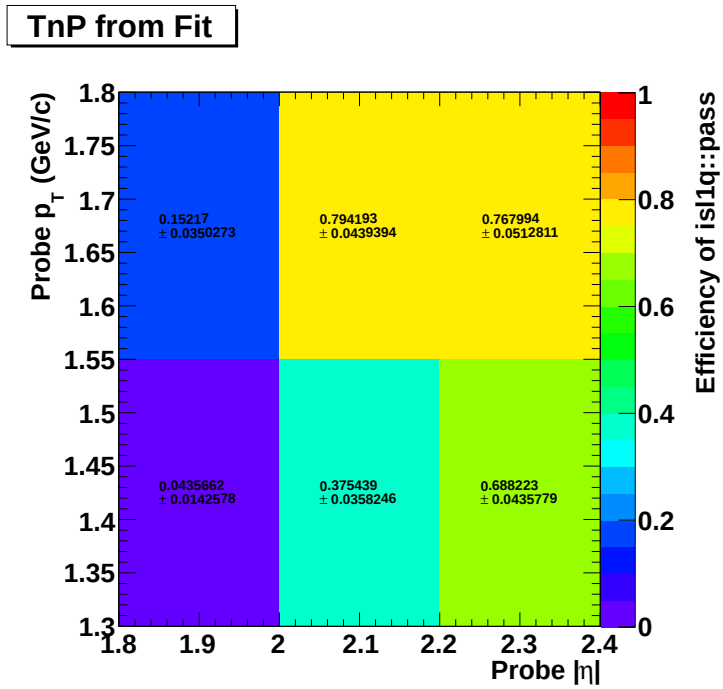

Figure 3.16: Muon trigger efficiencies in p_T and η bins from the tag and probe method.

The average dimuon trigger efficiency for each dimuon $(p_T, |y|)$ bin was calculated by averaging the efficiency of dimuon candidates in each bin. The dimuon trigger efficiency ranges from ~~$\approx 50\%$ to 87~~about 50% to 90%. As expected the J/ψ trigger efficiency increase with rapidity since the longitudinal momentum of the J/ψ is given $p_Z = M_{J/\psi} \cdot sinh(y)$. Thus J/$\psi$ mesons at forward rapidity distribute more momentum to their daughter muons which therefore have a greater chance of punching through into the muon chamber. The average trigger efficiency was multiplied by the acceptance and reconstruction efficiency from the MC to produce a total factor for both efficiency and acceptance.

The total combined efficiency and acceptance factor coherent J/ψ between $2.0 \leq |y| \leq 2.2$ was found to be $\approx 5\%$. The acceptance factor of roughly 7% from the MC was found to be the main contributor to the total efficiency. The interplay of the polarization of the J/ψ and the material in detector drive down the efficiency by creating an effective momentum threshold for detection (see Section 1.1). The reconstruction efficiency of the daughters range between 20%-60% for muons in the defined detectability range. The trigger efficiency for the detectable muons ranges from

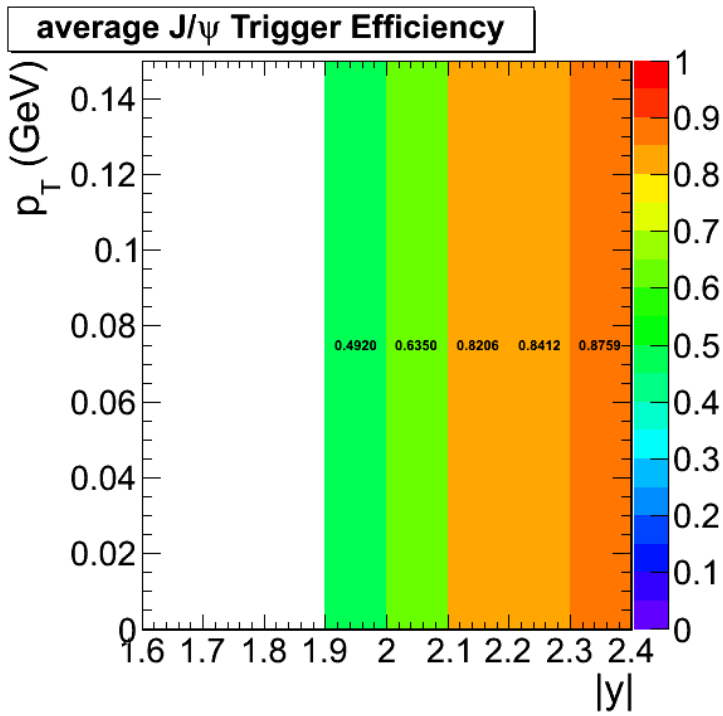

Figure 3.17: The trigger efficiency from tag and probe averaged over candidates in each (p_T,$|y|$) bin.

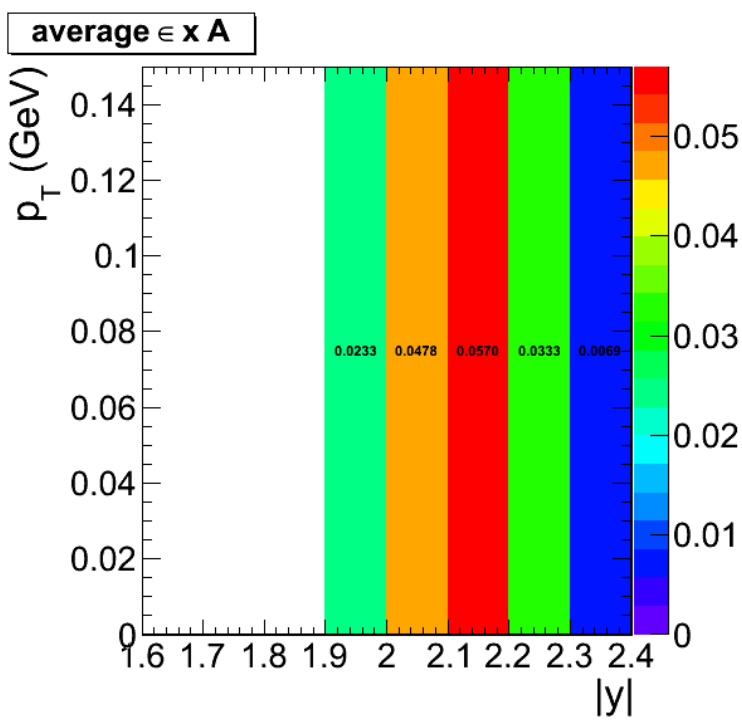

Figure 3.18: The acceptance times averaged trigger efficiency from tag and probe.

ZDC Side	N_{events}	N_{trig}	ε_{ZDC}
ZDC^+	73028	71706	0.9819 ± 0.005
ZDC^-	76132	71859	0.9439 ± 0.005

Table 3.3: ZDC trigger efficiencies for ZDC reconstruction method 1 and 2

30%-80% depending on p_T.

3.5.2 ZDC trigger efficiency

As discussed in Section 1.4, the trigger labeled "L1ZDCOr and Pixel Track" in Table 1.2 was used to measure the ZDC trigger efficiency. This trigger required either a ZDC^+ or ZDC^- trigger, together with at least one pixel track. The veto on the BSC minimum bias trigger, as in the physics triggers, was applied offline. The BSC veto excludes events where BSCs from both sides of the interaction point are above threshold. This trigger was used in order to collect the most inclusive possible sample without using the minimum bias triggers designed to collect hadronic interactions.

This ZDC triggered sample suffers from a trigger bias. For example, a sample triggered by ZDC^+ would always produce a ZDC^+ trigger efficiency of one. To avoid this, a similar technique to tag and probe was used. Each event is either tagged as triggered by ZDC^+ or triggered by the ZDC^-. The ZDC^+ trigger efficiency is measured from the ZDC^- tagged sample, and vice versa.

To estimate the efficiency, the number of events with energy in ZDC^+ greater than the single neutron threshold, N_{events}, was measured. From this set of events, the number of events that also fire the ZDC^+, N_{trig}, was measured. The ratio between the number of single neutron events that fired the trigger and all single neutron events was taken as the estimate of trigger efficiency. The same procedure was applied for each side of the ZDC. The trigger efficiency was found to be 98% for ZDC^- and 94% for ZDC^+.

3.6 Systematic ~~checks~~uncertainties

Table 1.6 shows the systematic errors that were estimated. The method used to separate the coherent from the photon-photon process is the most dominant error. The ZDC reconstruction method used to estimate the neutron thresholds is the next most dominant, followed by the method used to estimate the HF noise threshold.

systematic	uncertainty in %
Template fit ~~normalized~~ normalization	+9.5% -12%
ZDC trigger efficiency	2.2%
ZDC reconstruction	2.9%
HF noise threshold	+1.3% -3.4%
MC acceptance	1.1%
Total systematic	8.1%

Table 3.4: Summary of systematic uncertainties

3.6.1 HF noise threshold

The way in which the HF noise distribution is measured effects the event selection and therefore the final candidate ~~yeild~~yield. This cut plays a significant role in rejecting hadronic events. In Table 1.4 the importance of cutting on HF noise is evident. The HF noise cut rejects nearly 1/5 of the remaining events. The systematic uncertainties on the HF noise requirement is important for this reason.

The most fine grained data from the HF detectors are called RecHits. There is one RecHit per phototube on HF. The RecHit signal is calibrated in GeV, and no noise subtraction is done. The CaloTowers are formed from geometrical groups of RecHits. They are the first stage of the CMS jet trigger and perform some noise suppression.

The default HF noise cut required that the maximum RecHit energy from both HF+ and HF- be less than 3.85 GeV. This cut was designed to accept 99% of the noise events, see Fig. 1.3. The stability of this cut was tested by

1. Summing CaloTowers instead of RecHits

2. Making separate cuts on HF- and HF+

3. Tightening the threshold so that only 98% or 97% noise events passed the cut.

Table 1.7 shows the noise thresholds for RecHits and CaloTowers for both the combined HF+ and HF- calorimeters and the individual calorimeters when 99% of noise events are accepted. Table 1.10 compares the threshold for the cases when 99%, 98% and 97% of noise events are accepted. The number of J/ψ events remaining after these cuts is shown in EXPANDED TABLE. The efficiency corrected numbers are also shown. The fractional systematic error is then estimated by finding the maximum and minimum deviation from the default method. The systematic uncertainty from this method is calculated to be +1.3% -3.4%.

Object type	HF (GeV)	HF^- (GeV)	HF^+ (GeV)
RecHits	3.85	3.25	3.45
CaloTowers	4.25	3.25	3.75

Table 3.5: HF noise theresholds for various noise measurement methods.

Object type	Combinded HF threshold	Two-sided thresholds
RecHits	298	290
CaloTowers	302	288

Table 3.6: Candidate yields below 1.05 GeV p_T for various HF noise cuts.

Table 3.7: Values of the energy cuts for the HF calorimeter for RecHit and CaloTower in GeV.

%	E_{RecHit} GeV	$E_{CaloTower}$ GeV
99	3.85	4.25
98	3.25	3.75
97	2.95	3.25

3.6.2 Template fit normalization

The p_T template fit depends on the functions chosen for the fit to the mass distribution. As described in Section 1.5, the similarity of the of the p_T distribution for the coherent and photon-

Table 3.8: Number of dimuon candidates with p_T <1.05 when changing HF calorimeter cuts for RecHit and CaloTower.

%	RecHit cut	CaloTower cut
99	298	302
98	287	294
97	284	280

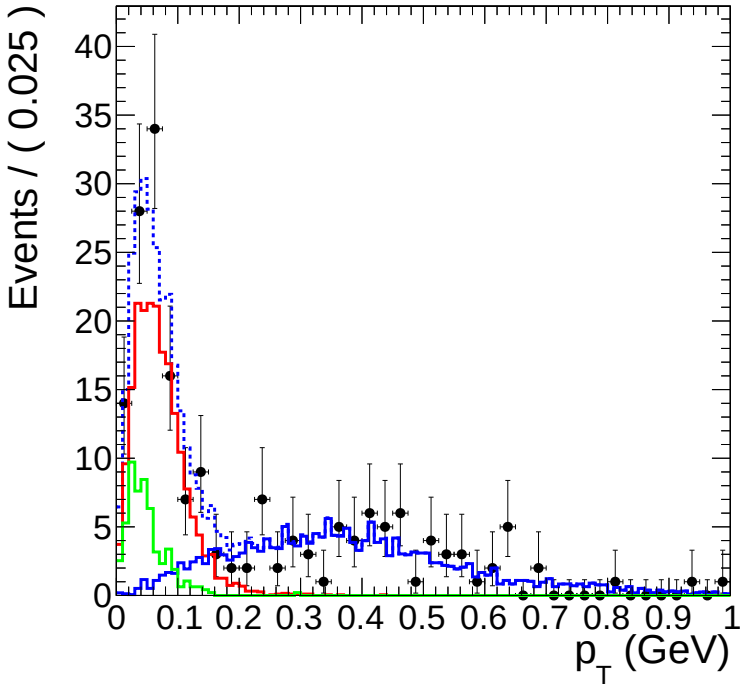

Figure 3.19: Coherent, incoherent, and photon-photon process p_T template fit to data.

photon process make the contributions from the two process difficult to separate from the p_T distribution alone. The mass distribution was used to distinguish between these two processes. In turn, the p_T becomes dependent on the mass fit.

The systematic uncertainty due to the choose of functions used to fit the mass distribution was estimated by varying the signal and background functions. The contribution to the background from the mass fit was used to fix the contribution from the photon-photon process in the p_T template fit. Two functions were used to describe the signal, a Gaussian, and a Crystal ball function. The background was fit to a linear function, a 2nd order polynomial, and a 2nd order Cheby-Chev polynomial. The resulting variation on the coherent contribution was used to as an estimate of this

systematic effect.

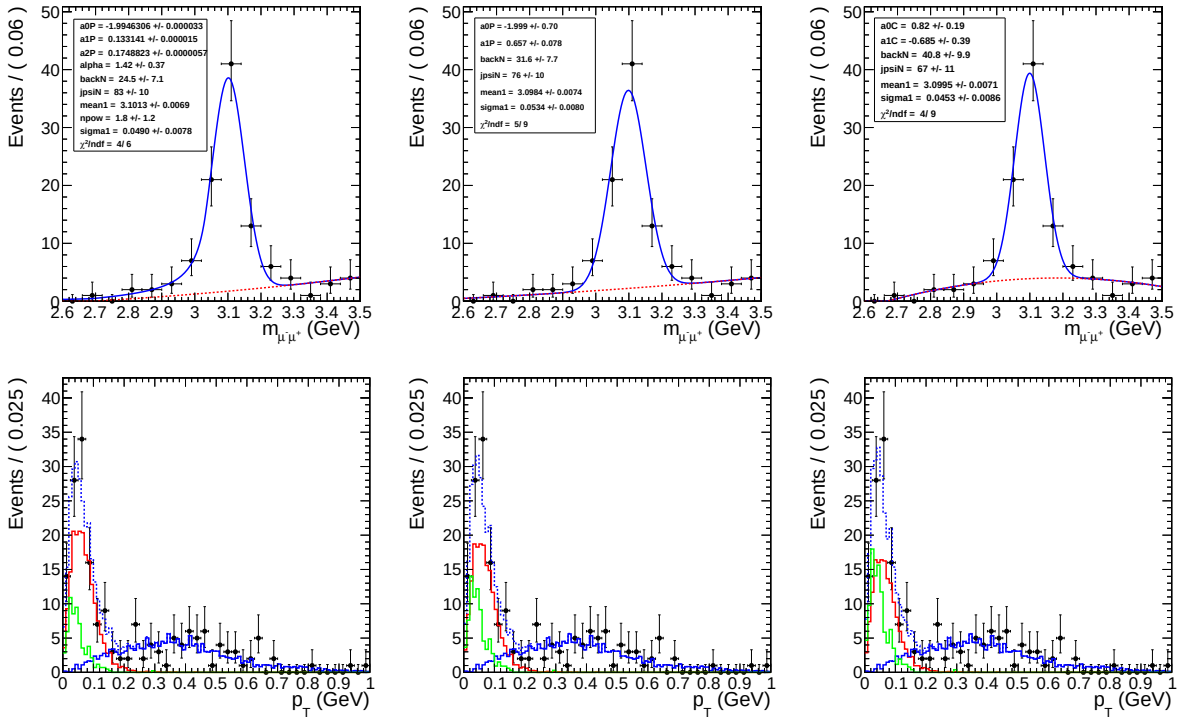

Figure 3.20: Various mass distribution fits and the corresponding p_T template fit.

Moving from left to right in Fig 1.20, the contribution from the photon process increases. The χ^2 pre degree of freedom is similar between the three fits indicating a similar goodness of fit. On this basis, neither fit is preferred. The left most fit uses a Crystal Ball function to account for the radiative decay of the final state daughters of the J/ψ. The low mass exponential portion however picks up background events and overestimates the J/ψ contribution. The right most plot fits the background to a 2nd order Cheby-Chev polynomial. Because the Cheby-Chev peaks just below the J/ψ peak, this fit overestimates the background and in turn underestimates the signal contribution. The Gaussian fit with a linear background however does a reasonable job of fitting both the background and the signal.

From these three fits an upper and lower bound of the systematics due the choice of fit functions was estimated. The difference between the Gaussian-Linear fit and the Crystal Ball-polynomial fit was taken as an upper bound. The difference between the Gaussian-Linear fit and the Gaussian-Cheby-Chev fit was taken as a lower bound. The overall systematic uncertainty due to the choose

of mass fit functions is found to be +9.5% -12%.

3.6.3 Mass fit

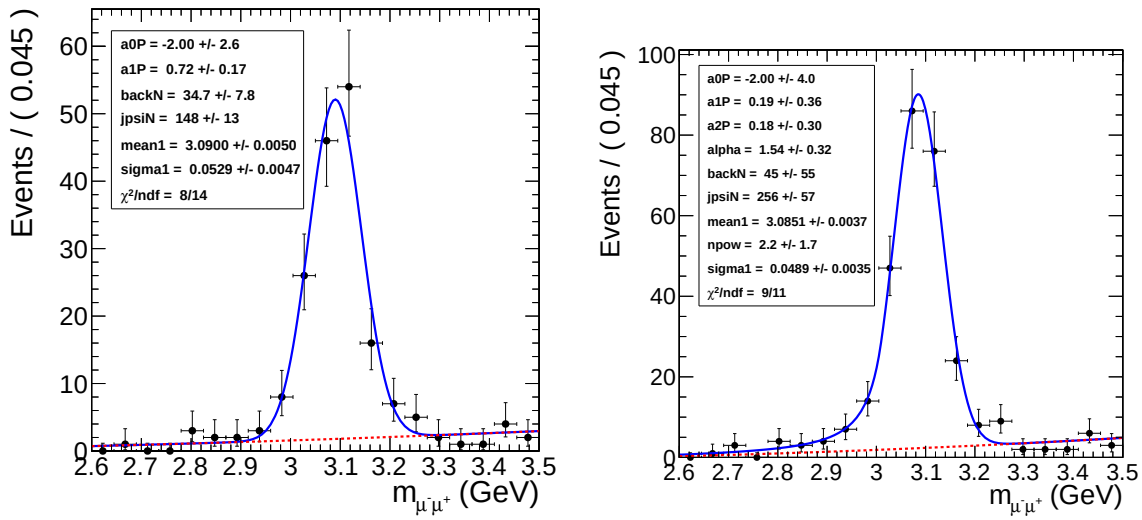

Figure 3.21: Mass fit to J/ψ using Gaussian (Left) and Crystal Ball (Right) for the signal and a polynomial for the background

Fig. 1.21 demonstrates the small dependence the raw J/ψ yield has on the fitting function. Both fit functions agree well, with reduced χ^2 values below one. The Crystal ball fit give an upper estimate for the J/ψ yield. The Gaussian fit gives an lower estimate. The main difference comes from the lower mass tails. In the Crystal ball fit the lower tail is considered to be signal due to shifting of the mass spectrum to lower mass due to radiation from the final state muons. In the Gaussian fit the lower mass tail is considered to be background and the signal is sharper.

As check on the simultaneous p_T and mass fit, the mass fit is done using mass templates from STARlight.

3.6.4 MC acceptance

The MC derived acceptance correction factors depend on the input physics generator. The underlaying p_T distribution was assumed to be correctly described by STARlight for the coherent cross

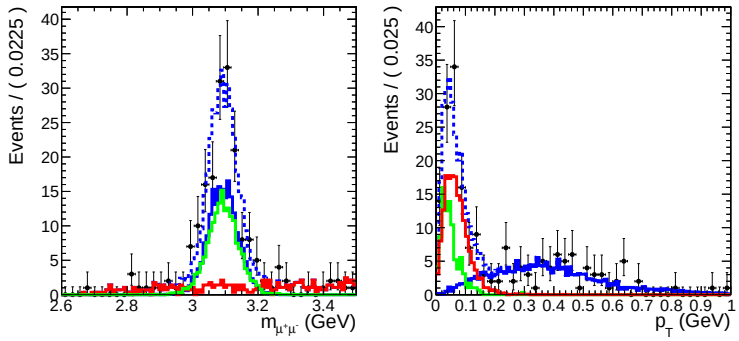

Figure 3.22: Simultaneous fit to the mass and p_T using mass templates for the mass fit.

section measurement. To estimate the effect of changing the underlaying p_T distribution on the acceptance measured from the MC, the incoherent sample was used to correct the coherent yield. By using the broader p_T distribution of the incoherent process, an estimate of acceptance measurements dependence on the assumed shape of the p_T distribution was obtained. The systematic uncertainty due to the dependence of the acceptance correction on the p_T distribution of the input physics generator was estimated by the difference between the correction factors from the coherent and incoherent MC samples. Half the difference was used as the estimate and was found to be 1.1%.

The effect of polarization was estimated by correcting by the acceptance for an unpolarized J/ψ sample.

3.6.5 ZDC reconstruction

An additional method for estimating the ZDC neutron thresholds was used to estimate the systematic errors on the threshold measurements. This additional method, used in previous ZDC measurements, differs in the way the signal time slices are used to calculate the signal from each channel. In the standard method, the signal is taken from the sum of time slices 4, 5, and 6. To estimate the event by event noise pedestal the sum of time slice 1 and 2 are used. The signal for an individual ZDC channel is then calculated as the sum of the signal time slices minus the sum of the noise time slices weighted by a factor of 3/2 to account for the differing number of noise

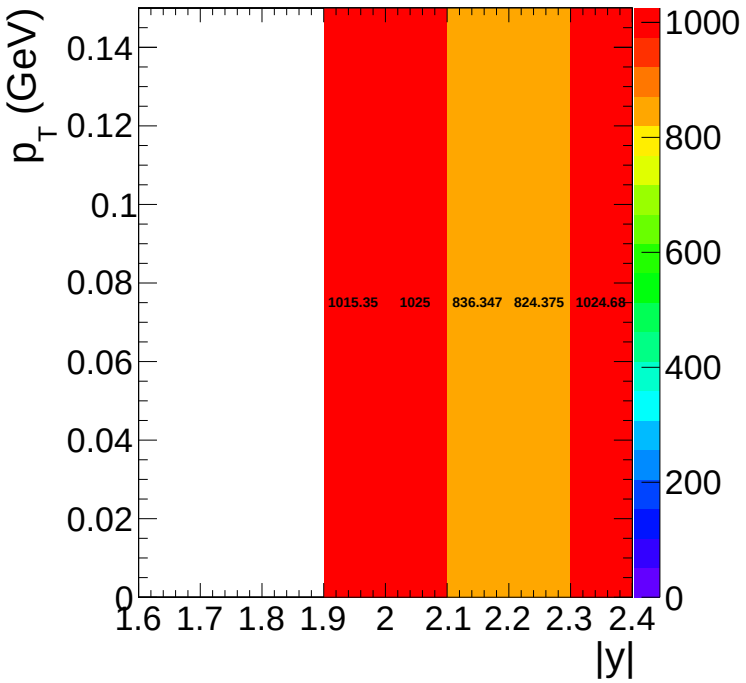

Figure 3.23: Yields corrected by the MC incoherent acceptance map.

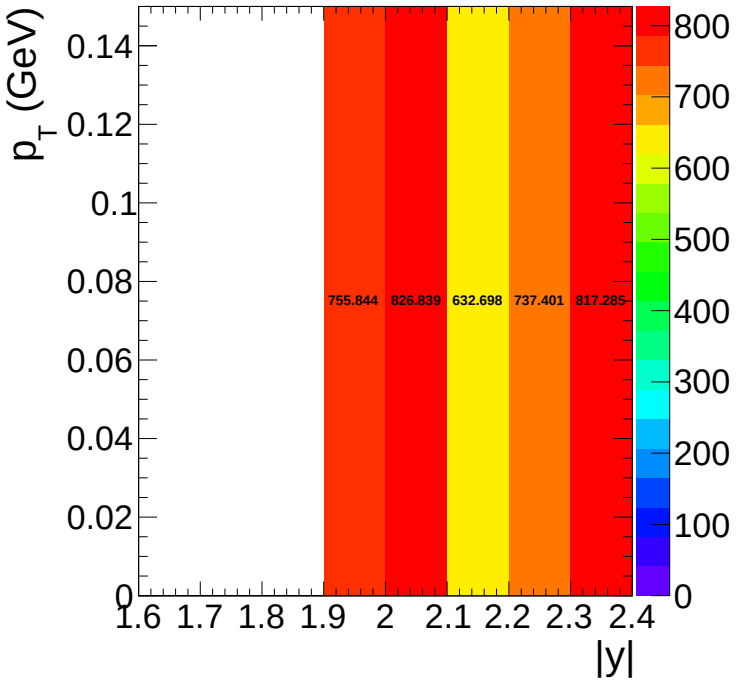

Figure 3.24: Yields corrected by an unpolarized J/ψ sample.

versus signal time slices. The advantage of the standard method is that by using multiple signal and noise time slices the signal and noise are effectively averaged reducing time slice to time slice fluctuations. However, by using time slices 1 and 2 for measuring the noise, the noise can only be measured half the time due to unmeasurable negative fluctuations of the dominant low frequency component of the noise.

As in the new method described in Section 1.4, the standard method combines the channels to create a signal measurement from the whole of each side of the ZDC, one measurement for ZDC^+, and one for ZDC^-. The noise subtracted signal from each of the HAD channels are added together. Then the EM section channels are summed. The EM section is weighted by a factor of 0.1 as in the new method. After the weighting the EM and HAD channels are added to each to create one measurement for ZDC^+ and another measurement for ZDC^-.

Fig. 1.25 shows the spectra for ZDC^+ and ZDC− using the standard method. The same fit used for the new method is applied to standard method. As in the new method, the single neutron threshold is set to 2σ below the mean from the fit to the one neutron peak. The multi-neutron threshold was set to 2σ above the one neutron peak.

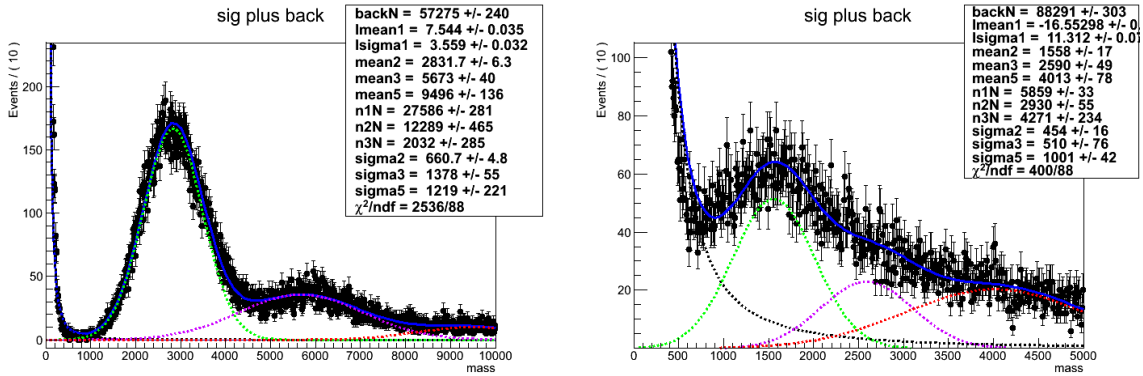

Figure 3.25: Fit to charge spectrum from ZDC^- (left) and ZDC^+ (right) using the standard reconstruction method

The systematic uncertainty due to the ZDC reconstruction method are estimated from the difference between the UPC J/ψ candidate yields. Both the reconstruction method and thresholds were changed to calculate the effect of the reconstruction method. The yields for the new and

ZDC Side	Reco Method	N_{events}	N_{trig}	ε_{ZDC}
(ZDC^+ or ZDC^-) and 1 pixel track				
ZDC^-	standard	72946	71688	0.982 ± 0.005
ZDC^-	new	73028	71706	0.982 ± 0.005
ZDC^+	standard	76137	71786	0.943 ± 0.005
ZDC^+	new	76132	71859	0.944 ± 0.005
(ZDC^- or ZDC^+), 1 pixel track, and L1 EG trigger				
ZDC^-	standard	613758	602123	0.9810 ± 0.0018
ZDC^-	new	614014	601863	0.9802 ± 0.0018
ZDC^+	standard	643905	602671	0.9360 ± 0.0017
ZDC^+	new	647888	603089	0.9309 ± 0.0017
(ZDC^- or ZDC^+), 1 pixel track, and L1 Muon trigger				
ZDC^-	standard	65466	63376	0.968 ± 0.005
ZDC^-	new	65543	63358	0.967 ± 0.005
ZDC^+	standard	71929	63512	0.883 ± 0.005
ZDC^+	new	72932	63582	0.872 ± 0.005

Table 3.9: ZDC trigger efficiencies for ZDC reconstruction method 1 and 2 for trigger sample which require a pixel track.

standard ZDC reconstruction method in the Xn0n break up were found to be 298 and 315 respectively. Half the difference between the two methods was used as an estimated of the systematic uncertainty. The systematic uncertainty due to the ZDC reconstruction method was found to be 2.9%.

3.6.6 ZDC trigger efficiency

The ZDC trigger efficiency measurement is sensitive to the underlying neutron distribution. The more neutrons that hit the ZDC, the higher the trigger efficiency will be. To estimate the effect the input sample has on the efficiency, the ZDC trigger efficiency was measured from five different samples. The Table 1.11 shows the results from the three samples, which require reconstruction a pixel track to reduce the contribution from noise. Both the new and standard ZDC reconstruction methods are shown for comparison.

The amount of electronic noise in the sample also effects the measurement. The more noise sits below the one neutron peak, the lower the efficiency is. In Table **??**, the Zero Bias sample

ZDC Side	Reco Method	N_{events}	N_{trig}	ε_{ZDC}
Zero Bias with ZDC timing cuts				
ZDC^-	standard	88676	84429	0.9521 ± 0.0046
ZDC^-	new	88480	84202	0.9517 ± 0.0046
ZDC^+	standard	59878	54728	0.9140 ± 0.0054
ZDC^+	new	60467	54733	0.9052 ± 0.0053
(ZDC^- or ZDC^+)				
ZDC^-	standard	30986	30333	0.9789 ± 0.0079
ZDC^-	new	31029	30339	0.9778 ± 0.0079
ZDC^+	standard	39178	30164	0.7699 ± 0.0059
ZDC^+	new	35703	30443	0.8527 ± 0.0067
Zero Bias				
ZDC^-	standard	109967	101598	0.9239 ± 0.0040
ZDC^-	new	110230	101561	0.9214 ± 0.0040
ZDC^+	standard	253241	86660	0.3422 ± 0.0013
ZDC^+	new	156336	87401	0.5591 ± 0.0024

Table 3.10: ZDC trigger efficiencies for ZDC reconstruction method 1 and 2 for samples that do not require a pixel track.

compared the Zero Bias sample with the timing cuts, which were described in the previous section, shows a significant increase in the estimated efficiency in the sample with reduced noise. The same increase is seen when comparing the ZDC triggered sample with the ZDC triggered sample that also requires a pixel track. The effect of the electronic noise is also present in the difference seen in using the two methods. As seen in Fig. 1.26, the new reconstruction method shows better separation of the one neutron peak from the electronic noise, in particular in ZDC^+ where the signal gain is lower. For this reason, the Zero Bias data, which contains the largest contribution from electronic noise, shows the most separation between the two methods and give the lowest estimate for the ZDC trigger efficiency.

The systematic uncertainty in the ZDC trigger efficiency due to the uncertainty in the underlying distribution was estimated by calculating the standard deviation of efficiency measurements in Table 1.11. The uncertainty in the ZDC trigger efficiency is taken to be 1% for ZDC^- and 4% for ZDC^+.

3.6.7 ZDC reconstruction method comparison

The new method relative to the standard method separates low signal from the noise more effectively for both sides of the ZDC. This is particularly important for ZDC$^+$ where the 1st HAD section had a lower gain than the other sections. The ZDC$^+$ and ZDC$^-$ signals near the one neutron peak using the standard and new reconstruction methods were plotted for comparison in Fig. 1.26. In Fig. 1.26, the shrinking of width of the noise peak around zero in the new method versus the old

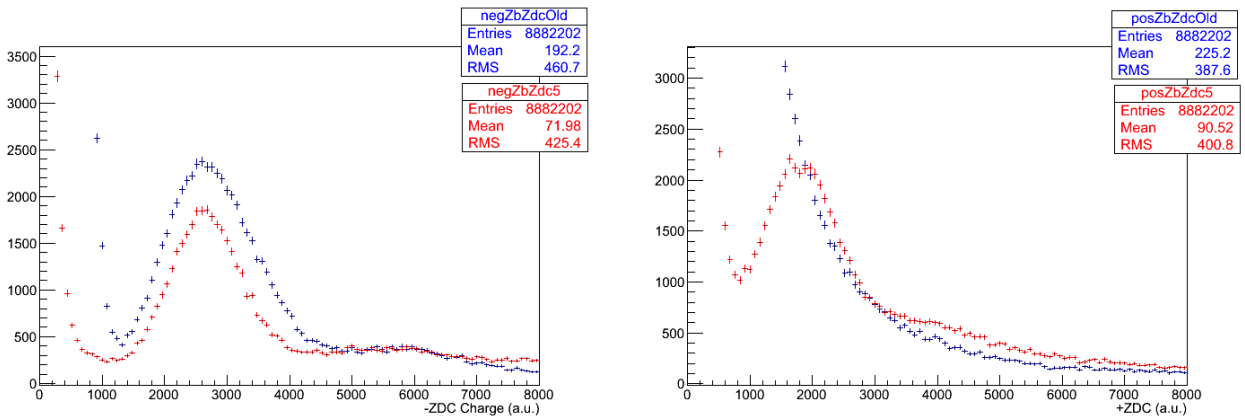

Figure 3.26: Comparison of the new ZDC reconstruction method and the standard method for ZDC$^-$ (left) and ZDC$^+$ (right).

method is apparent for both ZDC$^+$ and ZDC$^-$. For the standard method no single neutron peak is resolved in ZDC$^+$, whereas the single neutron peak is resolved using the new method.

Timing cuts were applied to enhance the signal relative to the background in order to resolve the one neutron peak in ZDC$^+$ using the standard method. Because the products of the collision are synced with time slice 4, noise can be rejected by selecting channels where the maximum signal falls into time slice 4. The noise will have no preferred time slice (see Fig. 1.4). Using this fact, signal can be preferably selected by requiring that the hadronic channels of the ZDC have a peak signal in the fourth time slice. Through these timing cuts the single neutron peak was recovered using the standard reconstruction for ZDC$^+$.

To examine the effectiveness of the timing cuts, event by event noise subtraction was removed from the standard reconstruction. The signal from each channel was taken from time slices 4,5, and 6 with out subtracting 1 and 2. The signal spectrum from ZDC$^-$ was then plotted with the

result shown in Fig. 1.27. As each additional hadronic channel is required to have a maximum

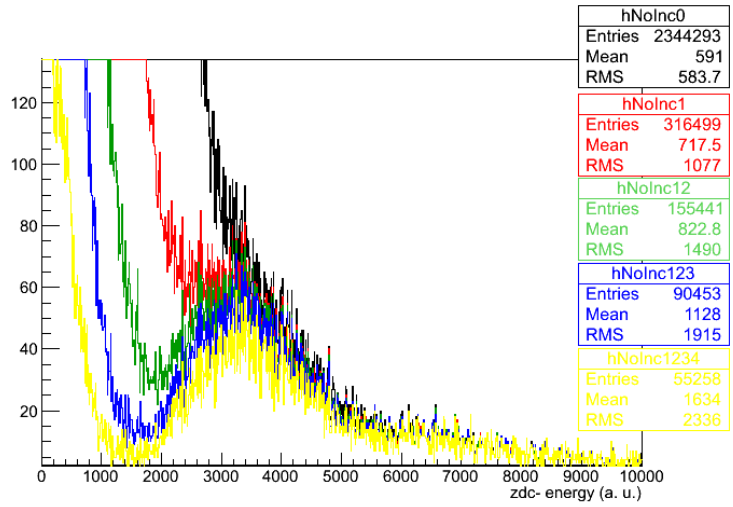

Figure 3.27: Effects of requiring in-time signal in successively more ZDC hadronic channels, no timing, at least one, at least two, at least three, and all four HAD channels have a maximum signal in the fourth time slice.

signal in the fourth time slice, the single neutron peak emerges. Fig. 1.27 demonstrates that the single neutron peak can be recovered from the noise using timing cuts alone.

Using the standard noise subtraction method, the same signal that emerges from the timing cuts alone appear without timing cuts. Fig. 1.28 confirms that both noise subtraction and the

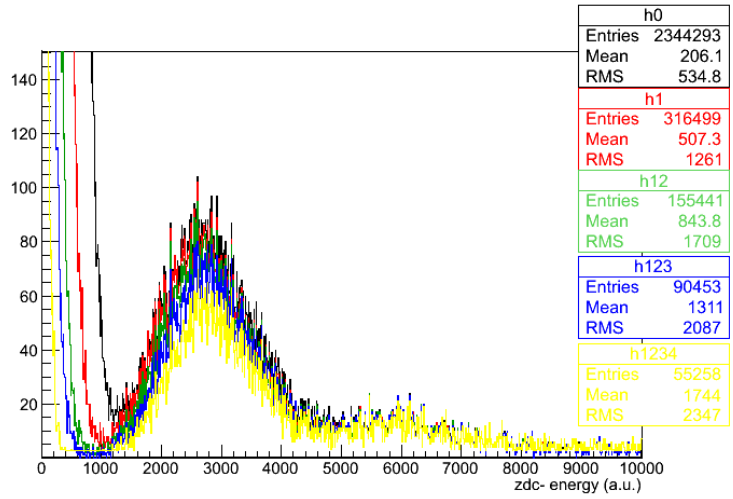

Figure 3.28: Effect of ZDC signal timing requirements after noise subtraction.

timing requirement produce the same signal. This gives confidence that the signal is not an artifact

of either cut, but the true neutron signal.

Fig. 1.28 and Fig. 1.26 demonstrate the consistence of the using timing cuts and noise subtraction to enhance the signal neutron peak. Fig. 1.28 confirms the legitimacy of the timing requirement method in ZDC^- by showing the that the same signal emerges from the noise subtraction method as the timing method. Fig. 1.26 demonstrates the corresponds between the new noise subtraction method and the standard method on in ZDC^- where signal is better separated from the electronic noise. This allows for confidence that the signal seen in ZDC^+ using the new method is the one neutron peak.

3.6.8 Tag and probe

The main purpose for fitting the mass spectra to estimate the efficiency is to separate the background from true signal. The background may not have the same efficiency as the signal, so separating the two is important if this is the case. In the tag and probe fit the signal peak from the J/ψ resonance is fit to the probes, passing probes, and failing probes alike (see Fig. 1.15). The signal shape, if from the same physical signal, will be identical in each of the three distributions. The background is for the passing and failing probes is fit using different parameters for the background because the background may come from different physical processes than the signal or non-physical sources like combinatorial backgrounds or misidentified fake particles. When the background comes from sources other than the physical signal, the background may give an efficiency estimate that is lower than the signal.

The trigger efficiency measured by the tag and probe method depend on the fitting functions use to estimate the background and signal contributions. Depending on what functions is used to fit the spectra, the amount of amount of background can be over or underestimated and effect the efficiency measurement. To estimate this effect, the tag and probe efficiencies were additionally measured by counting probes in the J/ψ mass window. The whole mass window is used to estimate the efficiency including all the events from the mass side bands. In this way, a worst case scenario estimate is given where all background events are included as signal.

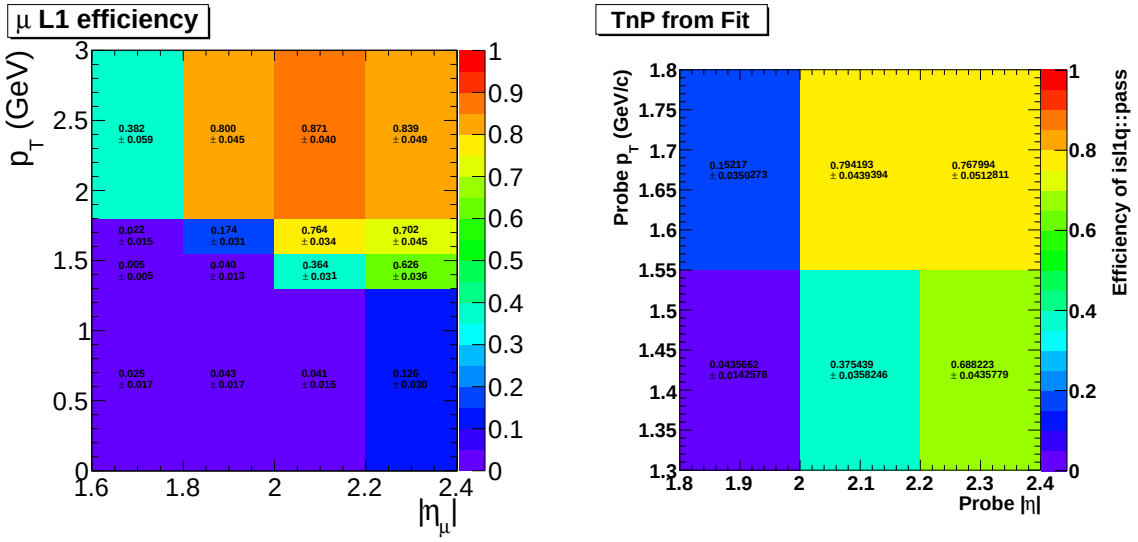

Figure 3.29: Tag and probe trigger efficiencies from counting (left) compared to fitting (right)

From Fig. 1.29 it is apparent that the choice of fit function and therefore the amount of background from the mass side bands is included in the signal measurement has very little effect on the tag and probe efficiency measurement. The small effect of including the side bands is due to the side bands being comprised mostly of photon-photon events. Because this background is neither decays from other particles like pions nor is it non-physical background like combinatorics, the efficiency for muons from the sidebands are nearly identical to J/ψ signal. The photon-photon process directly produces two muons just like the J/ψ, therefore efficiency estimated from the side bands has little effect on the measurement because of this similarity. The counting and fitting trigger efficiency measurements agree within statistcal uncertainties, so this uncertianty was taken to be negliable.

3.6.9 MC vs Data compairson

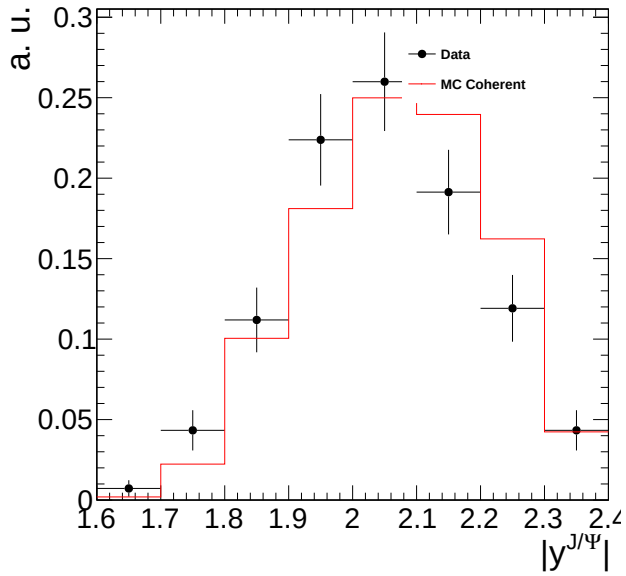

Figure 3.30: Comparison of the of the dimuon rapidity distributions between coherent MC sample and Data.

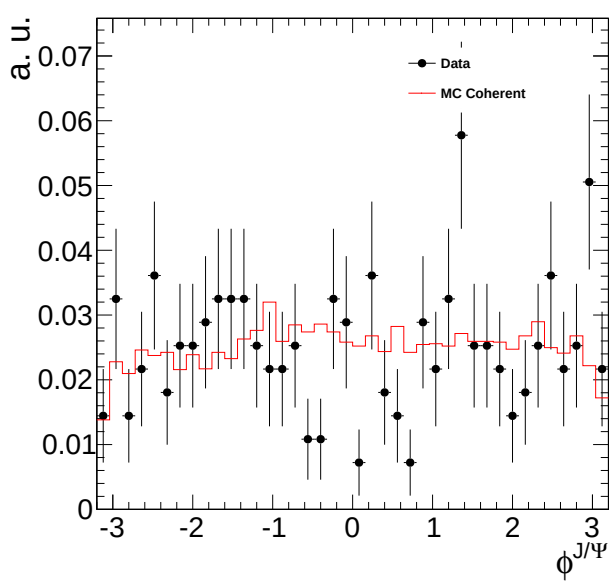

Figure 3.31: Comparison of the of the dimuon φ distributions between coherent MC sample and Data.

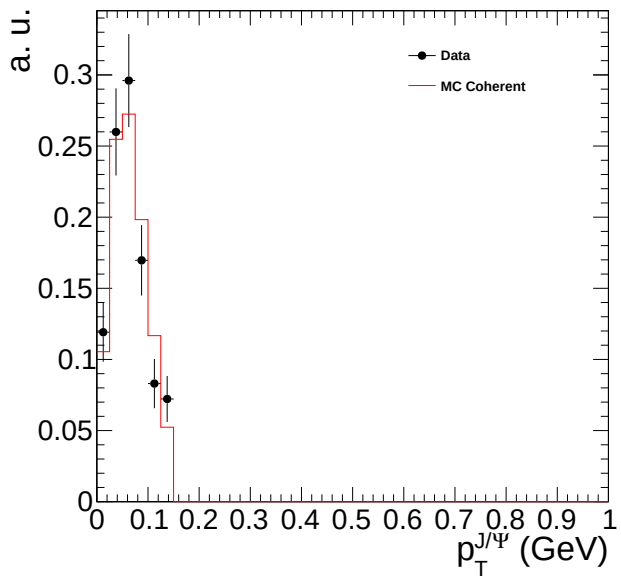

Figure 3.32: Comparison of the of the dimuon p_T distributions between coherent MC sample and Data.